JGR Oceans

RESEARCH ARTICLE
10.1029/2026JC024013

A Phenoregion Approach to Understanding Chlorophyll-a Seasonal Cycles and Interannual Variability in the South-West Indian Ocean

Aline Arens[1], Pierrick Penven[1], Fanny Chenillat[2], Stéphane Pous[3], Fialho Nehama[4], and Bernardino S. Malauene[5,6]

[1]University Brest, CNRS, IRD, Ifremer, Laboratoire d'Océanographie Physique et Spatiale, IUEM, Plouzané, France, [2]Actimar S.A.S., Brest, France, [3]Sorbonne Université, CNRS, IRD, MNHN, Laboratoire d'Océanographie et du Climat: Expérimentations et Approches Numériques (LOCEAN-IPSL), Paris, France, [4]Universidade Eduardo Mondlane, ESCMC, Quelimane, Mozambique, [5]Instituto Oceanográfico de Moçambique (InOM), Maputo, Mozambique, [6]Institute for Coastal and Marine Research (CMR), Nelson Mandela University, Gqeberha, South Africa

Abstract The South-West Indian Ocean (SWIO) displays marked spatial variations in physical forcings, driving in turn distinct seasonal biogeochemical regimes. Mesoscale eddies in the Mozambique Channel drive large-scale redistribution of nutrients and plankton, while eastern Madagascar waters are highly oligotrophic. However, the spatial organization and diversity of biogeochemical seasonal cycles across the SWIO remain insufficiently characterized on the basin scale. This study examines the seasonal and interannual variability of surface chlorophyll-a (Chl-a), used as a proxy for primary production. A phenoregion approach is employed, involving the grouping of areas exhibiting similar Chl-a phenology, that is, bloom timing (austral winter and/or summer) and the number of blooms per year (0, 1, or 2). 22-year of weekly satellite-derived Chl-a from the OC-CCI data set was used to generate normalized climatological seasonal cycles, which were subsequently clustered using a k-means algorithm. This approach identifies six distinct Chl-a phenoregions across the SWIO. Winter blooms dominate the basin and are likely associated with mixed-layer deepening and enhanced vertical nutrient supply, leading to temporally stable phenoregions. In contrast, summer blooms are restricted to coastal regions and south-eastern Madagascar, coinciding with enhanced terrestrial nutrient inputs during the wet season. In the Mozambique Channel, Chl-a exhibits limited seasonal variability, likely reflecting strong eddy-driven exchanges between coastal and offshore waters. Interannual analysis reveals stable phenoregion cores with consistent seasonality, while their boundaries exhibit variability, highlighting contrasts between persistent and highly intermittent biogeochemical regimes. The results obtained provide a basin-scale framework for linking physical dynamics to ecosystem variability in the SWIO.

Plain Language Summary Phytoplankton are microscopic algae that form the base of marine food webs. Their growth varies seasonally and is influenced by ocean circulation and the availability of nutrients. The South-West Indian Ocean is characterized by significant variations in these processes across different regions. Using 22 years of satellite observations of surface chlorophyll-a, a common indicator of phytoplankton biomass, we examined how phytoplankton abundance changes throughout the year. Based on the timing and number of annual peaks, we identified six regions with distinct seasonal chlorophyll-a patterns. While most of the region experiences a significant increase during the austral winter, summer peaks are primarily observed near the coast and in the south-east of Madagascar. In the Mozambique Channel, however, chlorophyll-a shows weaker seasonality than in the surrounding regions. While the regional patterns are generally stable over time, their boundaries vary from year to year, indicating differences in interannual variability across the basin. By clearly distinguishing areas exhibiting consistent seasonal behavior from those with more sporadic patterns, this study offers a systematic description of phytoplankton seasonality in the South-West Indian Ocean, providing a foundation for future research into the physical and biogeochemical processes that govern it.

Key Points:

- Six phenoregions are identified in the South-West Indian Ocean based on satellite chlorophyll-a bloom timing (season) and frequency
- Winter blooms dominate; summer blooms occur in coastal influenced regions; weak seasonality in Mozambique Channel
- Low interannual variability in low latitudes and the Mozambique Channel contrasts with highly intermittent southeast Madagascar

Supporting Information:

Supporting Information may be found in the online version of this article.

Correspondence to:

A. Arens,
aline.arens@univ-brest.fr

Citation:

Arens, A., Penven, P., Chenillat, F., Pous, S., Nehama, F., & Malauene, B. S. (2026). A phenoregion approach to understanding chlorophyll-a seasonal cycles and interannual variability in the South-West Indian Ocean. *Journal of Geophysical Research: Oceans*, *131*, e2026JC024013. https://doi.org/10.1029/2026JC024013

Received 12 JAN 2026
Accepted 18 MAR 2026

Author Contributions:

Conceptualization: Aline Arens, Pierrick Penven, Fanny Chenillat, Stéphane Pous, Fialho Nehama, Bernardino S. Malauene
Data curation: Aline Arens
Formal analysis: Aline Arens, Pierrick Penven, Fanny Chenillat, Stéphane Pous, Fialho Nehama, Bernardino S. Malauene
Funding acquisition: Pierrick Penven
Investigation: Aline Arens
Methodology: Aline Arens, Pierrick Penven, Fanny Chenillat, Stéphane Pous, Fialho Nehama, Bernardino S. Malauene
Project administration: Pierrick Penven

1. Introduction

The South-West Indian Ocean (SWIO) extends along the south-east African coast (study area: 5–30°S, 30–60°E; Figure 1). The island of Madagascar delimits the Mozambique Channel (MZC), which forms a corridor between Madagascar and Africa Mainland. The SWIO is a highly complex and turbulent region (Chelton et al., 2011; Halo, Backeberg, et al., 2014; Penven et al., 2014; Quartly & Srokosz, 2004), characterized by a western boundary

Resources: Aline Arens
Software: Aline Arens
Supervision: Pierrick Penven, Fanny Chenillat, Stéphane Pous, Fialho Nehama, Bernardino S. Malauene
Validation: Aline Arens
Visualization: Aline Arens
Writing – original draft: Aline Arens, Pierrick Penven, Fanny Chenillat, Stéphane Pous, Fialho Nehama, Bernardino S. Malauene
Writing – review & editing: Aline Arens, Pierrick Penven, Fanny Chenillat, Stéphane Pous, Fialho Nehama, Bernardino S. Malauene

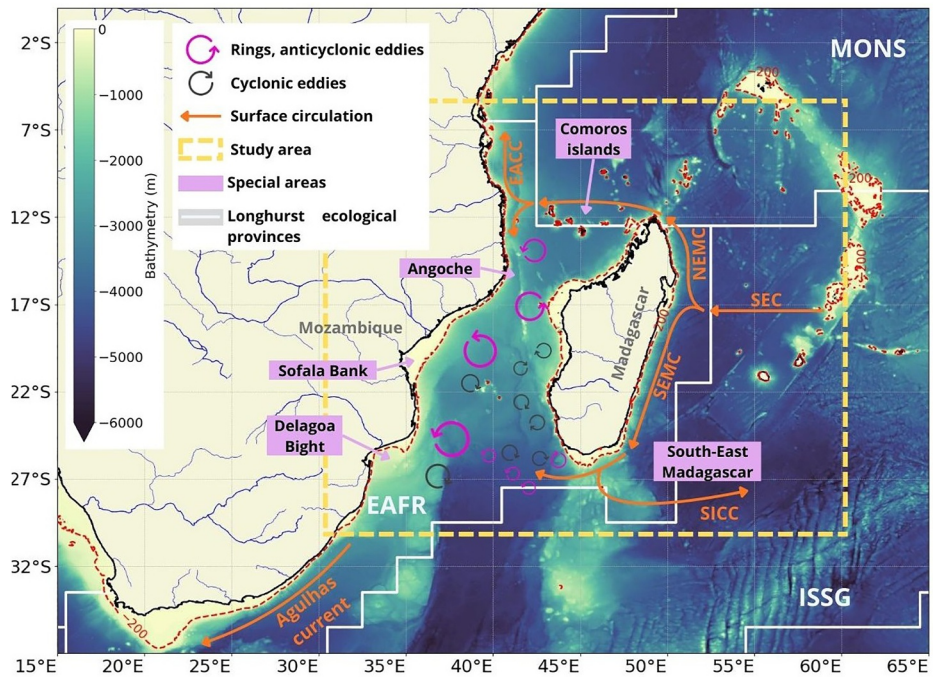

Figure 1. Study area showing the South-West Indian Ocean (SWIO) bathymetry (in m). The 200-m isobath is shown as a red dashed-line. The major rivers are represented (in blue line). Longhurst (1998) provinces are labeled in white: EAFR (Eastern Africa Coastal Province), ISSG (Indian South Subtropical Gyre Province) and MONS (Indian Monsoon Gyre Province). Main currents (adapted from Schott et al. (2009)) are represented in orange: South Equatorial Current (SEC), North-East Madagascar Current (NEMC), South-East Madagascar Current (SEMC), East African Coastal Current (EACC), South Indian Counter Current (SICC), Agulhas Current. Major turbulent areas are illustrated with pink arrows for anticyclonic eddies and with black arrows for cyclonic eddies. Areas of interest are indicated in purple.

circulation which generates contrasting environmental conditions (Lévy et al., 2007; Longhurst, 1998). As surrounding populations rely heavily on fisheries for their protein supplies (R. Van der Elst et al., 2005; R. P. Van der Elst et al., 2009), studying these ecosystems, starting from the base of the marine food chain—phytoplankton—is particularly relevant to address societal needs (Le Borgne et al., 2011).

As in most regions, phytoplankton displays seasonal variability, primarily driven by the seasonal cycle of environmental conditions, including temperature. Light and nutrients are needed to allow photosynthesis. If the growth of phytoplankton exceeds grazing, phytoplankton accumulates and a seasonal bloom can occur (Le Borgne et al., 2011). The phenology of phytoplankton blooms, defined by their seasonal timing and intensity, exerts ecosystem-wide effects. As it varies considerably between regions, it requires dedicated examination.

Nutrient availability within the photic layer depends on three main processes (Bristow et al., 2017): (a) vertical supply from deep waters through mixing or upwelling, (b) lateral inputs from external sources such as rivers, coastal waters, or atmospheric deposition, and (c) local remineralization of organic matter. Nutrient-rich coastal waters can travel offshore and alongshore by lateral advection through filaments around anticyclonic eddies (Malauene et al., 2024; Moore et al., 2007; Penven et al., 2025; Quartly & Srokosz, 2004). These coastal waters can also be trapped in the core of cyclonic eddies (José et al., 2016), which supply the offshore region with nutrient and biological materials (Chenillat et al., 2016). Geostrophic cyclonic eddies are often associated with a doming shape of isolines, including nitrocline, which could help to keep nutrient-rich water at the base of the photic layer, favoring higher Chl-a values (Chenillat et al., 2024).

The SWIO lies along the western boundary of the Indian subtropical gyre. Subtropical gyres are typically oligotrophic (Dai et al., 2023), with low nutrient availability and reduced surface primary production (Lamont, Barlow, & Brewin, 2018). In the SWIO, phytoplankton communities are dominated by picophytoplankton (Lamont, Barlow, & Brewin, 2018), and primary production is largely nitrate-limited (Koné et al., 2009). In such oligotrophic environments, remineralization alone is too low to sustain phytoplankton growth; vertical and

horizontal physical processes strongly control the depth of the nutricline (Oglethorpe et al., 2025). In such oligotrophic tropical regions, variations in mixed layer depth (MLD) are therefore a key driver of seasonal Chl-a variability: deepening of the mixed layer, often in winter, can episodically enrich the photic zone with nutrient-rich deeper waters (Signorini et al., 2015).

Circulation in the SWIO is primarily driven by the South Equatorial Current (SEC), which flows westward as part of the Indian Ocean monsoon system (Schott & McCreary, 2001). Reaching Madagascar, the SEC splits into the North-East Madagascar Current (NEMC) and the South-East Madagascar Current (SEMC) (Lutjeharms, 2006; Figure 1). The NEMC reaches the Comoros Islands and is deflected by the African coast, forming large anticyclonic eddies in the north of the MZC, called rings due to their typical vorticity structure (Halo, Backeberg, et al., 2014). The Mozambique rings flow southwards, down the MZC, making this place one of the most turbulent areas in the world (Chelton et al., 2011; Halo, Backeberg, et al., 2014; Penven et al., 2014). Smaller cyclonic eddies develop along the eastern side of the channel (Halo, Backeberg, et al., 2014; Schouten et al., 2003) and in Delagoa Bight (Cossa et al., 2016). The detachment of the SEMC south of Madagascar produces anticyclonic and cyclonic eddies that propagate westward toward Africa (Halo, Penven, et al., 2014; Quartly & Srokosz, 2004; Siedler et al., 2009). These mesoscale features shape marine ecosystems, from phytoplankton (José et al., 2014) to higher trophic levels, including pelagic fishes, cetaceans, and birds (Barlow et al., 2014; Tew-Kai & Marsac, 2009; Weimerskirch et al., 2004).

Consistent with this circulation complexity, several productive hotspots have been identified in the SWIO: the Sofala Bank under the influence of the Zambezi River discharge—increased in summer during wet season—(Malauene et al., 2018; Nehama & Reason, 2014, 2015a), the upwelling near Angoche in the northern Mozambique Channel (Malauene et al., 2014), the Delagoa Bight which host a semi permanent cyclonic structure (Cossa et al., 2016; Lamont et al., 2010; Quartly & Srokosz, 2004; Sá et al., 2013), the upwelling south of Madagascar (Machu et al., 2002) associated with favorable winds (Ramanantsoa et al., 2018) and with the detachment of the SEMC (José et al., 2016), and the intermittent south-east Madagascar summer bloom extending from the east coast of Madagascar (Dilmahamod et al., 2019; Longhurst, 2001; Srokosz et al., 2004). Island mass effects could also be expected around archipelagos (De Falco et al., 2022; Messié et al., 2020; Raapoto et al., 2019), such as the Comoros, Glorioso Islands, and the Seychelles.

Several studies have attempted to regionalize bloom phenology, that is, to define phenoregions, using satellite data. Indeed, the emergence of ocean color remote sensing since 1997 gave access to a global coverage of surface Chlorophyll-a concentration (Chl-a). Chl-a is commonly used as a proxy for primary production, that is, the net accumulation of biomass resulting from photosynthesis (Coleman et al., 2004). Based on large-scale patterns in ocean circulation, nutrient dynamics, and phytoplankton productivity, Longhurst (1998) proposed ecological provinces on global scale. Three provinces were defined over the SWIO (Figure 1):

- The Eastern Africa Coastal (EAFR) province includes western boundary currents from northern Kenya to the southern tip of Africa and encompasses the MZC. Its biological response is mainly driven by the deepening of MLD.
- The Indian South Subtropical Gyre (ISSG) province covers the northern monsoon gyre. The winter bloom of ISSG is also related to the deepening of MLD.
- The Indian Monsoon Gyre (MONS) province covers the southern subtropical gyre of the Indian Ocean. Only a small increase in Chl-a characterizes the MONS due to the south-west monsoon.

However, the wide extent and generalized geometric shapes of these provinces could provide only a coarse representation of SWIO processes.

Subsequent studies refined this approach by classifying regions according to the onset and peak timing of the blooms (Lévy et al., 2006, 2007). Lévy et al. (2007) identified winter and summer bloom regimes on the scale of the Indian Ocean, highlighting the existence of two dominant bloom seasons whose relative importance varies across regions. They defined a *Tropical Band* characterized by an austral winter bloom due to the deepening of MLD. A south-east Madagascar bloom was detected in austral summer. The MZC was partly described as an area with low seasonality. However, basin-scale approaches marginally addressed the smaller-scale and highly dynamic processes that characterize the SWIO, particularly within the MZC.

More recently, clustering approaches have been applied to objectively define phytoplankton phenoregions at local (Ferreira et al., 2021; Krug et al., 2018; Riom et al., 2025), regional (D'Ortenzio & Dalcaì, 2009; Fendereski

et al., 2014; Huot et al., 2019) and global scales (Baudena et al., 2025; Nicholson et al., 2025; Racault et al., 2012). In the SWIO, Riom et al. (2025) used a k-means clustering algorithm to determine areas of similar characteristics to develop a BGC-Argo float deployment strategy. It provided a separation of the seasonal cycles of Chl-a blooms into four regions depending on their bloom timing. However, the study relied on a short Chl-a time series and excluded the MZC.

Because oceanic circulation in the SWIO shows substantial interannual variability driven by large-scale climate modes, including the Indian Ocean Dipole (IOD) or El Niño Southern Oscillation (ENSO; Currie et al., 2013; Palastanga et al., 2006), phenoregions are also expected to vary in time, as shown in the Mediterranean Sea (Mayot et al., 2016).

The state of the art highlights several persistent difficulties in describing phytoplankton phenology in the SWIO. The proposed regionalizations are often too coarse to account for the high spatial diversity and local processes, such as coastal processes, MLD forcing, and mesoscale remobilization in the MZC. Furthermore, the interannual variability of these phenoregions has never been characterized. In light of these gaps, this article addresses the following central questions: How are the seasonal cycles of Chl-a distributed in space and time in the SWIO? And how stable are the identified phenoregions in interannual terms?

To answer these questions, a long series of ocean color satellite data spanning 22 years (2002–2023) is analyzed. The calculation of normalized seasonal cycles from the Chl-a time series is performed and, subsequently, clustering methods are applied to group regions with homogeneous seasonal cycles, which are called phenoregions. The present analysis focuses on both the average shape of the seasonal cycles within each phenoregion and their interannual variability. Next, we relate these patterns to known physical processes (e.g., vertical mixing, coastal advection, and mesoscale dynamics) to suggest explanations for the observed differences.

The results reveal a comprehensive regionalization of the SWIO into contrasting phenological regions, including stable structures and others that exhibit significant variability. The MZC is identified as a particularly complex area, characterized by the diversity of seasonal signatures and their interannual variability. These findings enhance our comprehension of phytoplankton phenology in an oligotrophic and turbulent area, with implications for fisheries management and marine resource assessment. The methodology and data sets are described in Section 2. The analysis of phenoregions and their interannual variability is presented in Section 3, followed by a discussion in relation to physical processes in Section 4.

2. Material and Methods

2.1. Data Set

Satellite Chlorophyll-a surface concentration (Chl-a; in mg m^{-3}) was used as a proxy for phytoplankton biomass. Level 3 (L3) 8-day average Chl-a data, with a spatial horizontal resolution of 4 km, was extracted from the European Space Agency (ESA) Ocean Colour-Climate Change Initiative (OC-CCI) product (version 6.0, available online at http://www.esa-oceancolour-cci.org), on the study area (5–30°S, 30–60°E, Figure 1; https://doi.org/10.24381/cds.f85b319d). This product includes data from five sensors, combined to cover more than 20 years (Mélin et al., 2017; Sathyendranath et al., 2019): the Sea-Viewing Wide Field-of-View Sensor (SeaWiFS; 1997–2010), the Medium-Resolution Imaging Spectrometer (MERIS; 2002–2010), the MODerate resolution Imaging Spectroradiometer (MODIS; 2002–2019), the Visible Infrared Imaging Radiometer Suite (VIIRS; 2011–2019), and the Ocean and Land Colour Instrument (OLCI; SENTINEL-3A: 2016-present and SENTINEL-3B: 2018-present). Changes in satellite coverage can induce a loss of stationarity in the time series. To minimize this effect and ensure consistency, we restrict our analysis to Chl-a satellite data over the period 2002–2023, thus excluding the earlier SeaWiFS-only period, as recommended in Hammond et al. (2018). The waters in the study area are predominantly classified as Case I (Wei et al., 2022), which means that phytoplankton and their by-products are the main components. In contrast, Case II waters are influenced by additional independent constituents such as suspended particles and colored dissolved organic matter (CDOM) (Morel, 1988). Where the bathymetry is less than 200 m (see Figure 1), the nearshore band often falls into the Case II category (Lee & Hu, 2006; Matsushita et al., 2012; Wei et al., 2022). Since multi-captor processing of OC-CCI data has been optimized on Case I waters (Sathyendranath et al., 2019), we have excluded the continental shelf from our study.

2.2. Clustering Methods

The general strategy for studying SWIO bloom phenology, which is summarized in Figure 2, includes three main phases: preprocessing (Steps 1, 2, and 3), climatological phenoregion identification (Steps 4, 5, and 6), and interannual phenoregion identification (Step 7).

Detailed steps are as follows (see Figure 2):

- *Step 1: Raw data.* For each timestep, raw Chl-a map is extracted from L3 products, therefore including cloud gaps. To exclude Case II waters from the study, we apply a bathymetry-based mask for areas shallower than 200 m (see the 200-m isobath in Figure 1).
- *Step 2: Spatial clouds gaps filling.* Following the method of Lévy et al. (2006), for each map of each timestep, missing data pixels are filled by applying a mobile spatial average three consecutive times; The treated pixels are filled with the mean of the values in a 9×9 pixel window, weighted in $1/r^2$, with r being the distance from the center to the window.
- *Step 3: Temporal clouds gaps filling.* For each pixel, weekly time series are smoothed by running a 5-week temporal mobile average (Lévy et al., 2006).
- *Step 4: Normalized seasonal cycle.* A weekly climatological seasonal cycle is computed on each pixel. To focus on the shape of the seasonal cycles (number of blooms and timing), climatological seasonal cycles are normalized by their maximum value, hence reducing the effects of high concentration differences on the SWIO scale (D'Ortenzio & Dalcaì, 2009).
- *Step 5: Clustering with k-means.* Climatological seasonal cycles are regionalized with a k-means clustering algorithm. The optimal number of clusters k is determined as the first value with an acceleration of the inertia gain smaller than 5% (based on Krug et al. (2018); see details in Supporting Information S1). $k = 4$ is obtained.
- *Step 6: Climatological Phenoregions.* Climatological Phenoregions (referred as CP in the figures) are obtained in the k-means clustering algorithm with $k = 4$. For each climatological phenoregions, the associated seasonal cycle is obtained by averaging the seasonal cycle of each pixel within the climatological phenoregions.
- *Step 7: Interannual association with correlations.* Interannual variability of bloom phenology is assessed by assigning each pixel from each year to a climatological phenoregions, following the method of Mayot et al. (2016). To build this association, we choose the Pearson correlation instead of the Chebyshev distance, as it enables comparison of the full seasonal cycle rather than only peak values (Derrick et al., 1993). For each pixel, the climatological phenoregions exhibiting the highest Pearson correlation coefficient with its yearly seasonal cycle is selected (Figure 2, step 7a). Pixels are then retained only if they meet two criteria: a significant level of 95% ($p - value < 0.05$) and a sufficiently high correlation coefficient ($coeff > 0.4$). Otherwise, the pixel is labeled "NS," "not significant or $coeff < 0.4$" (Figure 2, step 7b). After processing all pixels, a phenoregion map is obtained for years from 2002 to 2023, referred to as Interannual Phenoregions (or IP in the figures).

To describe the seasonal cycle of each climatological phenoregion, a series of metrics is computed, following Ferreira et al. (2021). The *peak* of the bloom is defined as the local maximum of the seasonal cycle. The *onset* of the bloom is defined by the last intersection of the median with the seasonal cycle during the increasing phase (before the peak of the bloom). For the peak and the onset of the bloom, Chl-a values and the associated week are recorded. The annual average of Chl-a concentration over the entire seasonal cycle is also calculated.

3. Results

3.1. General Patterns of Chl-a

First, the aim here is to describe the general spatial and seasonal variations of Chl-a in the SWIO to highlight its contrasted patterns. The yearly concentrations of Chl-a averaged over 22 years (2002–2023) in the SWIO are presented in Figure 3a.

The SWIO has a clear oligotrophic signature in most of the subtropical gyre. The central part of the gyre, which extends to the east of Madagascar, exhibits extremely low Chl-a values, typically below 0.1 mg m^{-3}. Moving toward the northern and western boundaries of the gyre, there is a slight increase in Chl-a (between 0.2 and 0.5 mg m^{-3}). In the central MZC—between the African coast and Madagascar from 10°S to 25°S—a slight

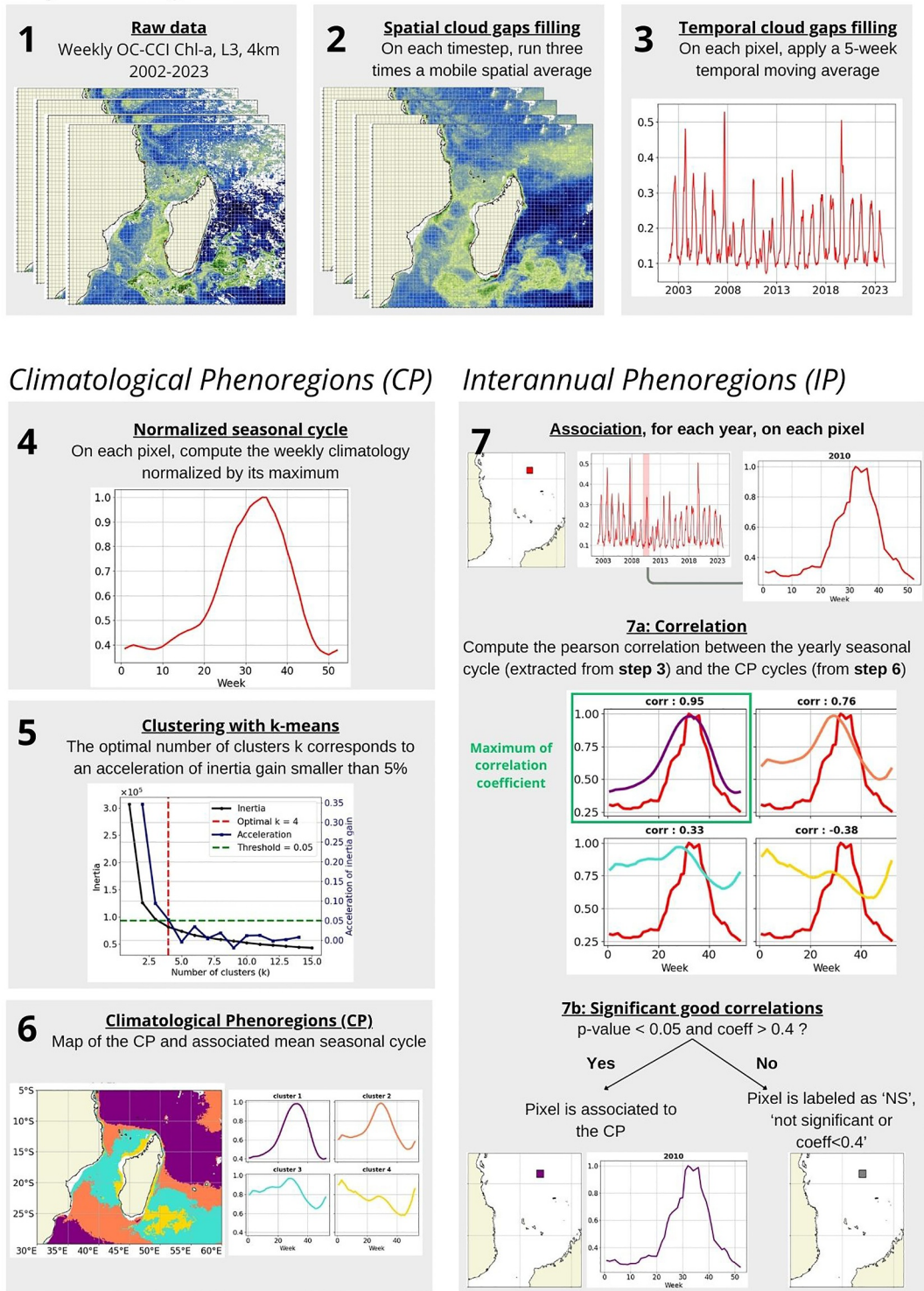

Figure 2. Schematic representation of the methodological steps. *Step 1:* Extraction of raw Chl-a data, containing cloud gaps, excluding coastal areas (bathymetry < 200 m). *Step 2:* Spatial cloud gaps filling. *Step 3:* Temporal smoothing on each pixel. *Step 4:* Normalization of climatological seasonal cycles. *Step 5:* Clustering with k-means, and optimal number of clusters *k* determination. *Step 6:* Map of Climatological Phenoregions (CP) and associated spatial mean seasonal cycle. *Step 7:* Interannual variability by associating the seasonal cycle from each pixel of each year to the most similar CP seasonal cycles defined at step 6, thanks to Pearson correlations (*Step 7a*) and threshold on p-values and correlation coefficients (*Step 7b*). See details in Section 2.2.

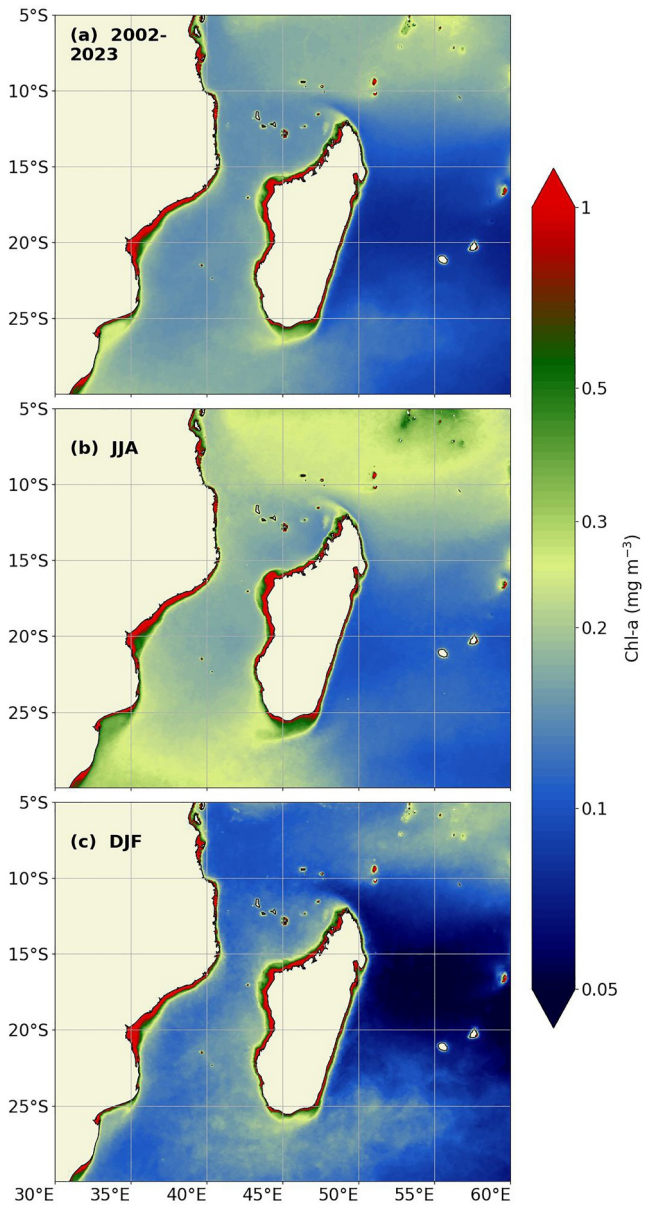

Figure 3. Mean Chl-a. Chl-a concentration (in mg m^{-3}) averaged over 2002–2023, (a) yearly, (b) during austral winter (JJA: June, July and August), and (c) during austral summer (DJF: December, January and February).

increase in Chl-a can also be observed, reaching 0.15–0.2 mg m^{-3}. Figure 3a illustrates an overall strong cross-shore gradient between productive coastal bands at the margins of the basin and the nutrient-poor open ocean.

Locally, high Chl-a concentrations can be seen at the detachment of currents from the northern and southern tip of Madagascar: in the south, the SEMC (see general circulation in Figure 1) is known to induce coastal upwelling south of Madagascar favoring phytoplankton production (Machu et al., 2002; Ramanantsoa et al., 2018); and in the north (north of 10°S), the Seychelles-Chagos thermocline ridge likely drives an increase in Chl-a concentration (Carr et al., 2025; Dilmahamod et al., 2016).

In contrast, the near-coastal regions display higher concentrations (>1 mg m^{-3}). Such coastal productive regions correspond to the continental shelf, around Madagascar and along the African coast, especially on Sofala bank (around 20°S) and in Delagoa Bight (26°S); they may be classified as Case II waters (Lee & Hu, 2006; Matsushita et al., 2012; Wei et al., 2022). As discussed earlier, the data processing algorithms in the satellite OC-CCI product are not optimized for Case II water (Sathyendranath et al., 2019); thus, such high coastal values cannot be associated with confidence to productive waters related to coastal nutrient enrichment or to increased dissolved organic matter in shallow waters. Higher concentrations are also observed around several small islands, particularly in the Comoros archipelago, but these areas are discarded for the rest of the analysis for the same reason.

On the seasonal scale, seasonal changes in phytoplankton biomass in the SWIO, in austral winter (June-July-August: JJA, called winter hereafter) and austral summer (December-January-February: DJF, called summer hereafter), are shown in Figures 3b and 3c, respectively. Several areas exhibit minimal changes between the two seasons, highlighting a low seasonality. For example, the center of the subtropical gyre, to the east of Madagascar, remains low in Chl-a concentration (< 0.15 mg m^{-3}) for both seasons. The MZC is also characterized by a weak seasonal cycle, maintaining relatively higher Chl-a concentrations on the SWIO scale, although a slight increase is noticeable in winter.

In contrast, other offshore areas exhibit clear seasonality. Chl-a concentrations north of 10°S reach values above 0.3 mg m^{-3} in winter (Figure 3b), contrasting with lower values in summer (< 0.1 mg m^{-3}, Figure 3c). Similarly, Chl-a concentrations south of 25°S vary from more than 0.3 mg m^{-3} in winter (Figure 3b) down to 0.2 mg m^{-3} in summer (Figure 3c). Both areas are dominated by higher Chl-a concentrations in winter. On the contrary, Chl-a concentrations to the south-east of Madagascar (22–30°S, 47–55°E) reach their maximum in summer, increasing from 0.1 in December to 0.2 mg m^{-3} (Figure 3c).

In summary, mean Chl-a concentrations underline contrasting patterns in the region with seasonal variations that will be examined using a phenoregion approach.

3.2. Climatological Phenoregions

To refine the description of Chl-a seasonal variability, a cluster analysis is applied on the seasonal cycles (Steps 4, 5, and 6 from Figure 2). The optimal number of cluster analysis (see Supporting Information S1) led to the definition of four phenoregions. Each phenoregion is characterized by a typical seasonal cycle (see Figure S2 in Supporting Information S1). Phenoregions are named on the basis of the timing of their main peaks as follows: Winter Bloom (WB), Summer Bloom (SB), Winter & Summer Blooms (WSB) and No seasonal Bloom (NB). Offshore areas have been gathered during clustering, despite their different amplitudes and distinct geographical

locations and their contrasting Chl-a concentration patterns (as shown in Section 3.1). This is due to the normalization by the maximum value of the cycles. This highlights a limit of the clustering method. Therefore, in order to provide a more comprehensive description of the range of processes at play, we have decided to divide the SB and NB phenoregions into two parts using geographical criteria as detailed in Text S3 of Supporting Information S1. It is important to note that the WSB phenoregion is treated as a single entity, even though it comprises several distinct subregions. In fact, these subregions exhibit a similar seasonal cycle and demonstrate no significant differences in amplitude (not shown). In the following sections of this article, we will thus discuss six phenoregions, called hereafter climatological phenoregions. The map of the repartition of the final six climatological phenoregions is represented in Figure 4a and their associated spatial mean seasonal cycles in Figures 4b–4g.

Characteristics of each climatological phenoregion such as area (in km^2), percentage of coverage, value (in mg m^{-3}), and timing (week and associated month) of bloom onset and peak, annual mean Chl-a (in mg m^{-3}) are summarized in Table 1 and detailed in the following subsections.

3.2.1. Winter Bloom (WB)

Within the WB phenoregion, Chl-a seasonal cycle is marked by a single maximum in winter (Figure 4b), with an onset in May and a Chl-a peak occurring in August with 0.228 mg m^{-3} (see Table 1). WB Chl-a seasonal cycle presents a relatively small envelope of variability among all the climatological phenoregions, underlying the spatial coherence of the signal.

The WB is the largest identified phenoregion, covering 42.56% of the SWIO and displaying medium productivity on the SWIO scale (mean Chl-a of 0.145 mg m^{-3}). This climatological phenoregion forms a large band north of Madagascar, from the eastern African coast to the eastern boundary of the domain, which corresponds to the *Tropical Band* identified by Lévy et al. (2007). A second area of the WB phenoregion is located south of Delagoa Bight (south of 25°S).

3.2.2. Summer Bloom (SB)

The SB phenoregion is the smallest climatological phenoregion, covering 6.13% of the SWIO, and is composed of 2 sub-regions (see the separation criteria in Text S3 of Supporting Information S1): SB-Coasts and SB-SEM (South-East Madagascar; Figure 4a).

SB-Coasts is a coastal band around almost all Madagascar, covering 2.13% of the SWIO. SB-Coasts is 50 km wide on the east coast, constrained to the east by the SEMC, and extends beyond the continental shelf at about 100 km off the west and north-west coasts.

SB-SEM is located in the south-east of Madagascar, and covers 4.00% of the SWIO. SB-SEM extends from Madagascar to the east, following the path of the South Indian Counter Current (cf. SICC in SWIO circulation in Figure 1). It shows the typical dendroid shape of the south-east Madagascar bloom with a central patch around [26°S, 51°E] from which multiple elongated arcs and squirts develop (Dilmahamod et al., 2019; Longhurst, 2001).

Chl-a seasonal cycles of both SB phenoregions are characterized by a single summer bloom, with an onset period in December and a peak in January (Figures 4f and 4g). However, it is noteworthy that in the 2019–2020 period, a significant unusual bloom occurred in the southeastern region of Madagascar. The occurrence of this event was both premature and uncommonly high concentrated (Gittings et al., 2024), thereby influencing the timing of the climatological bloom. Excluding this outlier from the analysis, the SB-SEM bloom onset occurs on average in week 1 and reaches its maximum in week 4, which is more consistent with the findings of (Srokosz et al., 2004).

The Chl-a seasonal cycles of each SB phenoregion differ strongly in concentration range, which provides a posteriori justification for their separation. In the SB-SEM subregion, in the south-east of Madagascar, the Chl-a concentration increases from 0.123 mg m^{-3} to 0.154 mg m^{-3}. In the SB-Coasts subregion, Chl-a concentrations increase from 0.218 mg m^{-3} to 0.276 mg m^{-3}, exhibiting a maximum value that is almost twice that observed in SB-SEM. Chl-a seasonal cycles of each SB phenoregion also differ by the width of their envelope of variability, five times wider for SB-Coasts.

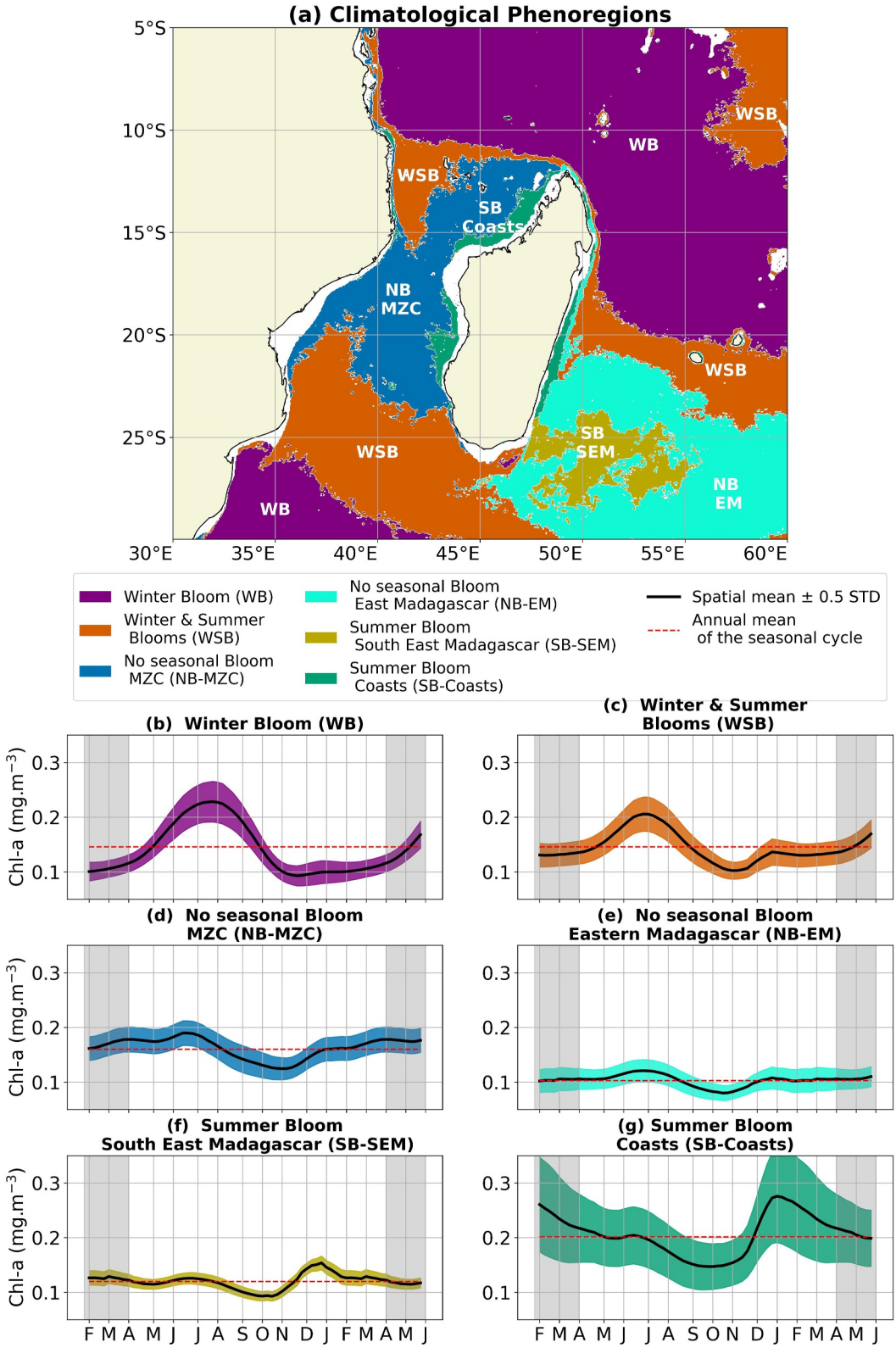

Figure 4. Climatological Phenoregions (CP). (a) Map of the phenoregions obtained from normalized climatological seasonal cycles, and (b–g) associated spatial mean of seasonal cycle (solid black curve) with the spatial standard deviation (shaded colored envelope). Annual mean is in red dashed line. Each colored referred to a CP: Winter Bloom (WB) is in purple, Winter & Summer Blooms (WSB) is in orange, No seasonal Bloom (NB) sub-regions are in dark blue (MZC) and light blue (EM, Eastern Madagascar) and Summer Bloom (SB) sub-regions are in yellow (SEM, South-East Madagascar) and green (Coasts).

Table 1
Climatological Phenoregions (CP) Characteristics

CP name	Area (10^6 km^2) coverage (%)	Onset value (mg m^{-3}) week (month)	Peak value (mg m^{-3}) week (month)	Chl-a mean (mg m^{-3})
WB	2.46	0.131	0.228	0.145
	42.56%	Week 18 (May)	Week 32 (August)	
WSB		0.136	0.206	0.145
	1.48	Week 14 (April)	Week 28 (July)	
	25.69%	0.102	0.136	
		Week 47 (November)	Week 2 (January)	
NB	0.63	0.163	0.190	0.160
MZC	10.93%	Week 8 (February)	Week 26 (June)	
NB	0.85	0.106	0.121	0.102
EM	14.69%	Week 19 (May)	Week 28 (July)	
SB	0.23	0.123	0.154	0.119
SEM	4.00%	Week 50 (December)	Week 2 (January)	
SB	0.12	0.218	0.276	0.201
Coasts	2.13%	Week 51 (December)	Week 3 (January)	

Note. Area of each phenoregion is given in km^2 with its corresponding coverage of the total area in percentage. Week number and associated month of bloom onset and peak are indicated with their associated value (in mg m^{-3}). Yearly mean values of climatological phenoregion seasonal cycle spatial mean are given in mg m^{-3}. Phenoregion names are given in Figure 4. EM and SEM stand for Eastern Madagascar and South-East Madagascar, respectively.

3.2.3. Winter & Summer Blooms (WSB)

WSB is the second largest phenoregion, covering a quarter of the total area (25.69%). The WSB is adjacent to the WB and NB-MZC regions, forming a transition zone. It is separated into four spatial areas, mostly following zonal jets in the average circulation.

One of the regions is located in the north-east corner of the study area, north of 12°S and east of 56°E, close to the Mascarene plateau. Another region represents a band between Madagascar, Réunion, and Mauritius islands around 21°S, following the southern border of the SEC (see general circulation in Figure 1). Two other parts are located north and south of the MZC, respectively. One region follows the NEMC in its crossing toward the African continent around 12°S (cf. SWIO circulation in Figure 1). It extends into the north-western side of the MZC, along the western part of the Comoros Gyre (Collins et al., 2016), in the generation area of the Mozambique Channel Rings (Halo, Backeberg, et al., 2014). Therefore, this subregion corresponds to the beginning of the anticyclonic rings corridor. The last region extends from the south of Madagascar to the Mozambican coasts around 23°S. Its western part is likely co-located with the end of the anticyclonic rings corridor of the MZC and with tracks of eddies generated from the south of Madagascar (De Ruijter et al., 2005; Halo, Backeberg, et al., 2014).

The Chl-a seasonal cycle of WSB is characterized by two blooms (Figure 4c). The first bloom occurs in winter, with an onset in April, peaking in July, to 0.206 mg m^{-3} of Chl-a. The winter bloom represents the main bloom and coincides with the bloom of WB, 4 weeks earlier. A second bloom occurs in summer, with an increase in Chl-a from November to January (peak at 0.136 mg m^{-3} of Chl-a). It coincides in timing with the SB blooms, but starting 3 weeks earlier. The overall yearly WSB mean Chl-a value is 0.145 mg m^{-3}.

3.2.4. No Seasonal Bloom (NB)

The NB phenoregion represents slightly more than a quarter of the domain (25.62%). The NB phenoregion has been split regarding its relative position to Madagascar (see the separation criteria in Text S3 of Supporting Information S1): The western NB is called NB-MZC (for Mozambique Channel) and the eastern NB is named NB-EM (for Eastern Madagascar). The separation is justified by their different range of Chl-a concentrations (Figure 3a). Each part represents about half of the NB phenoregion.

The western NB-MZC phenoregion covers 10.93% of the SWIO in a butterfly shape. One of the outgrowth is along the Mozambican coast from Angoche to the Sofala Bank; the other, larger than the previous one, extends over the eastern part of the MZC, along Madagascar, an area dominated by cyclonic eddies. It covers the eastern part of the Comoros Archipelago, which corresponds to the Comoros Gyre. The center part of the butterfly-shape corresponds to the middle part of the anticyclonic rings corridor (rings radii are greater than 100 km Halo, Backeberg, et al. (2014)), the northern and southern parts belonging to the WSB phenoregions. The NB phenoregion also includes Scattered Islands in the middle of the Channel: Bassas da India, Europa and Juan da Nova.

The eastern NB-EM, which covers 14.69% of the SWIO, is actually located in the south-east of Madagascar. NB-EM surrounds the SB phenoregion and is limited to the north and west by the WSB phenoregion.

The Chl-a seasonal cycle of NB phenoregions is almost constant throughout the year, with almost equal onset and maximum Chl-a values (Table 1): they do not present a clear seasonal bloom (Figures 4c and 4d). The two subregions differ in their relative Chl-a concentrations. The NB-MZC is the most productive, with a mean Chl-a concentration of around 0.160 mg m^{-3}, contrasting with Chl-a concentrations in NB-EM (remaining around 0.102 mg m^{-3}). They also differ in terms of envelope of variability: the MZC, characterized by a high level of mesoscale eddy activity, has a wider envelope than the NB-EM phenoregion.

To sum up, the seasonal cycles of the SWIO have been separated into six contrasted phenoregions. This spatial separation defines regions with similar biogeochemical properties, whose variations will be studied in the following sections.

3.3. Chl-a Concentration Variations

Now that the phenoregions are clearly separated, we can analyze in more detail the Chl-a concentration variability. The complete Chl-a times series averaged for each of these regions (Figure 5) are presented in Section 3.3.1. A particular focus on the MZC case is made in Section 3.3.2.

3.3.1. Chl-a Timeseries in Climatological Phenoregions

Time series of spatially averaged Chl-a for each climatological phenoregion are shown in Figure 5, together with their associated trend and their residual anomalies (obtained after de-trending and filtering the seasonal cycle). The Theil-Sen method (Akritas et al., 1995) is used in the calculation of trends as it is a non-parametric statistical method, which is less affected by outliers when compared with standard linear regression. The yearly running mean of residual anomalies is also computed for each phenoregion.

For each of these components (mean, trend and residual anomalies), we quantify the proportion of variance they explained in the full signal (Table 2). For each climatological phenoregion, the seasonal cycle patterns previously described can be mostly observed each year in the total signal (Figure 5, panels a1–f1), while interannual variability can be depicted in residual anomalies (Figure 5, panels a2–f2).

In the WB phenoregion (Figure 5a1), the annual recurrence of winter blooms is clearly visible in accordance with 90% of the total signal variability explained by the seasonal cycle (Table 2). Nevertheless, the amplitude of these blooms varies slightly from year to year, as highlighted by the fluctuations in the anomaly (Figure 5a2). The anomaly demonstrated a decrease from 2002 to 2008, an increase from the minimum in 2012 to the maximum in 2020, and subsequently, another decrease. The smallest blooms reached values below 0.2 mg m^{-3} in 2008, 2011, and 2015; the largest ones, 0.27 mg m^{-3} in 2003 and 2020. Between each bloom, the Chl-a concentration decreases to around 0.1 mg m^{-3} every year. There is no significant trend.

The two seasonal blooms of the WSB phenoregion are identifiable almost every year, the major one in winter and the smaller one in summer (Figure 5b1). Around 2/3 of the signal variability is explained by the seasonal cycle and the remaining by the residual anomalies (~40%), as the trend is not significant. Some interannual variations of the WSB blooms can be highlighted: in 2002, 2005, 2010, 2016 and 2017 the summer bloom is almost not existent; in contrast, in 2008 and 2020 the summer bloom has a greater amplitude than the winter one, especially in 2020 when the peak value reaches 0.48 mg m^{-3}. The 2020 bloom corresponds to two major bloom events in the south-east of Madagascar that extend largely over the domain. Winter bloom usually reaches a peak value of 0.2 mg m^{-3}.

The complexity of the NB-MZC phenoregion is confirmed by the percentage of variance explained (Table 2). 48.83% of the signal is explained by the residual, 48.32% by the seasonal cycle, and the remaining 2.06% by the

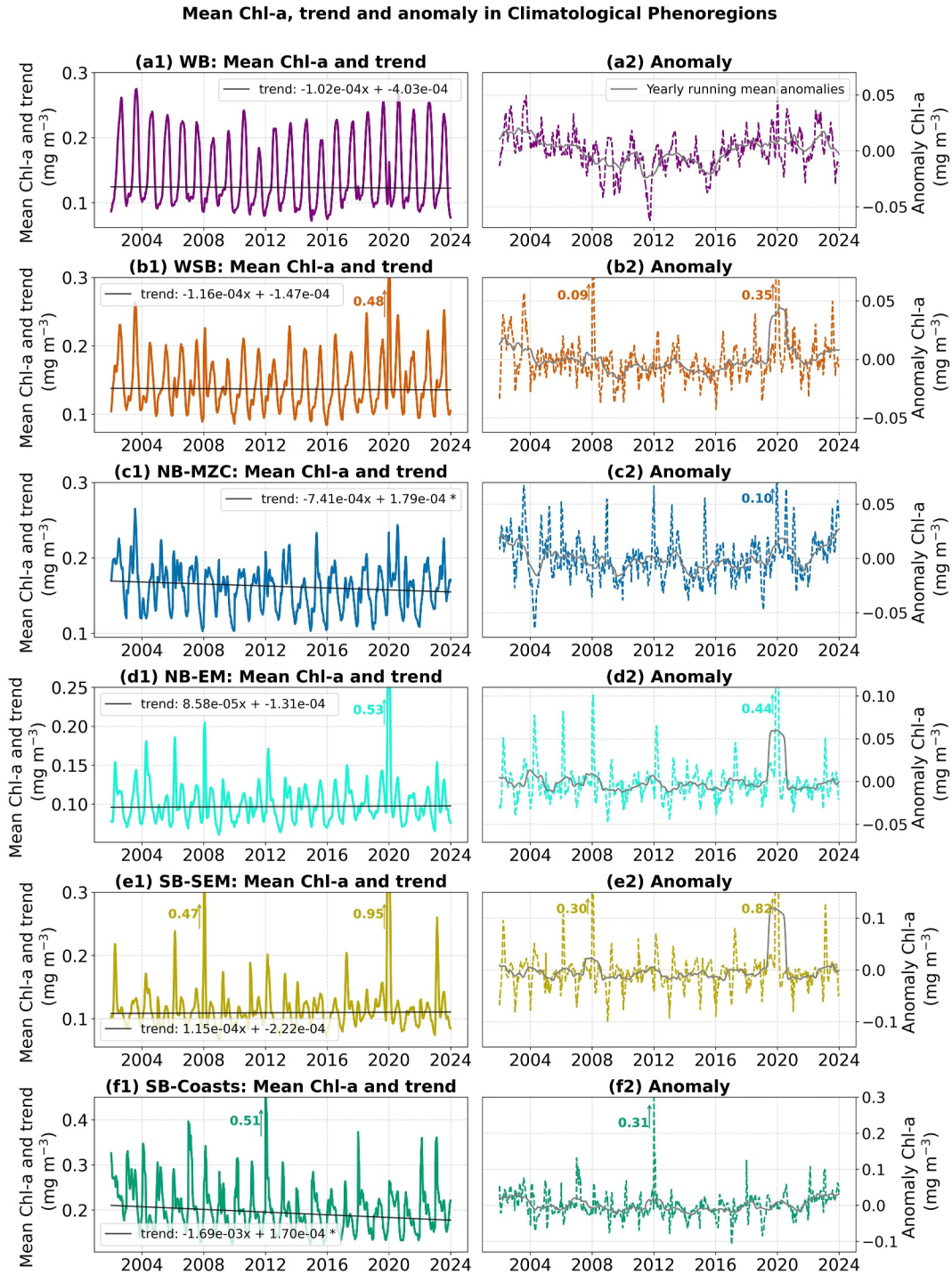

Figure 5. Chl-a time series, trend and anomaly. Left panels, (a1–f1), represent averaged Chl-a concentration time series (in mg m^{-3}), in each climatological phenoregion (colored curves) and the associated interannual trend (in mg m^{-3} $year^{-1}$, black lines). The trend equation, calculated with Theil-Sen method (Akritas et al., 1995), is shown in the legend, with a star (*) indicating trends that are statistically significant at the 95% confidence level. Right panels, (a2–f2) represent the residuals anomalies (i.e., de-trended and deseasonalized signal) (colored curves). A yearly running mean is shown in gray. For better readability, the *y*-axes are limited, and peak values are indicated next to the vertical arrows.

Table 2
Proportion of Variance Explained by Each Component: Trend, Seasonal Cycle, Residual for the Different Climatological Phenoregions (CP)

CP name	Trend (%)	Seasonal cycle (%)	Residual (%)
WB	0.01	**89.88**	10.11
WSB	0.02	**59.55**	40.51
NB-MZC	2.06	**49.83**	48.32
NB-EM	0.02	10.60	**89.26**
SB-SEM	0.01	5.70	**94.15**
SB-Coasts	3.17	**57.32**	38.53

Note. The higher proportion is indicated in bold.

trend. The weak seasonality and complexity of this area is also confirmed in Figure 5c with no clear, regular blooms. Indeed, unlike other offshore phenoregions, Chl-a concentrations never fall below 0.1 mg m^{-3} and stay close to 0.16 mg m^{-3}. The almost constant Chl-a concentrations over time makes the MZC the second most productive area after coastal areas. The region has a strong interannual variability with a statistically significant decreasing trend of -7.41×10^{-4} mg m^{-3} $year^{-1}$. To better describe this particular region, a focus is made in the following subsection (Section 3.3.2).

In the NB-EM phenoregion (Figure 5d1), Chl-a concentrations are highly variable, with the residual component explaining 89.26% of the total signal. Concentration values are generally between 0.1 and 0.15 mg m^{-3}, which is a relatively small range. Such small annual variability confirms the lack of seasonality in this sub-region associated with strong oligotrophic conditions (Lamont, Brewin, & Barlow, 2018). However, there are a few peaks with larger values, notably in 2008 and 2020, when the south-east Madagascar blooms (observed in SB-SEM) extend so far that high Chl-a concentrations reach this region.

For the SB-SEM phenoregion (Figure 5e1), the amplitude of the summer blooms varies greatly from year to year with anomalously positive productive years. This phenomenon can be attributed to the dominance of residual anomalies in the total signal, which accounts for approximately 95% of the observed variability. The most significant peaks occurred in 2002, 2006, 2008, 2012, 2017, 2020, and 2023. The 2020 bloom is much higher than the others, reaching a value of 0.95 mg m^{-3}. The spatial extent of this bloom, described extensively by Gittings et al. (2024), is such that it also manifests a signature in the WSB and NB-EM regions (Figures 5b1 and 5d1).

For the SB-Coasts (Figure 5f1), the production is higher than in the other regions with a clear unique bloom in summer. The seasonal cycle and the trend explain 57.32% and 3.17% of the total variance, respectively. A statistically significant trend of -1.69×10^{-3} mg m^{-3} $year^{-1}$ is observed. In 2012, a special high value was recorded, with a peak value of 0.51 mg m^{-3} (Figure 5f2).

Interannual variations might be related with large scale climate modes. To test this hypothesis, we computed Pearson correlations between monthly mean of Chl-a concentration anomalies of each phenoregion and climate indexes provided by the NOAA (National Oceanic and Atmospheric Administration) with a monthly temporal resolution. Correlations lagged by 0.5, 1, 1.5, and 2 years were also tested. Multivariate ENSO Index (MEI, available online https://www.psl.noaa.gov/enso/mei) illustrates the change from El Niño to la Niña events in the Pacific Ocean, inducing variations in wind and sea surface temperature. The Indian Ocean Dipole (IOD, available online https://psl.noaa.gov/data/timeseries/month/DMI/) accounts for the oscillation of sea surface temperatures in which the western Indian Ocean becomes alternately warmer and colder compared to the eastern part of the basin.

The interconnection of processes appear to be complex in the SWIO (De Ruijter et al., 2005; Palastanga et al., 2006; Schouten et al., 2002) and only a few correlations appeared to be significant. Monthly Chl-a anomalies in WB phenoregion present a 0.25 correlation with MEI with a lag of 1 year. The anomaly observed in NB-MZC phenoregion could be explained by IOD with a 0.18 correlation with a lag of 0.5 year. Finally, monthly Chl-a anomalies in SB-Coast are correlated with MEI with a correlation coefficient of −0.19 and −0.25 for 1 and 1.5 year lags, respectively. They also display a −0.2 correlation with IOD with 1.5 year lag. Correlations with other environmental variables (such as Eddy Kinetic Energy, EKE, or MLD) have been tested, but no significant correlations were found.

3.3.2. Chlorophyll Variations in the Mozambique Channel

As described previously and shown in Figure 5c, the MZC does not exhibit a clear seasonal bloom. The total signal is in fact equally explained by the seasonal cycle and the residual anomalies (Table 2). This makes the MZC a particular region, known to be one of the most turbulent in the world (Chelton et al., 2011; Halo, Backeberg, et al., 2014; Penven et al., 2014), which is interesting to focus on.

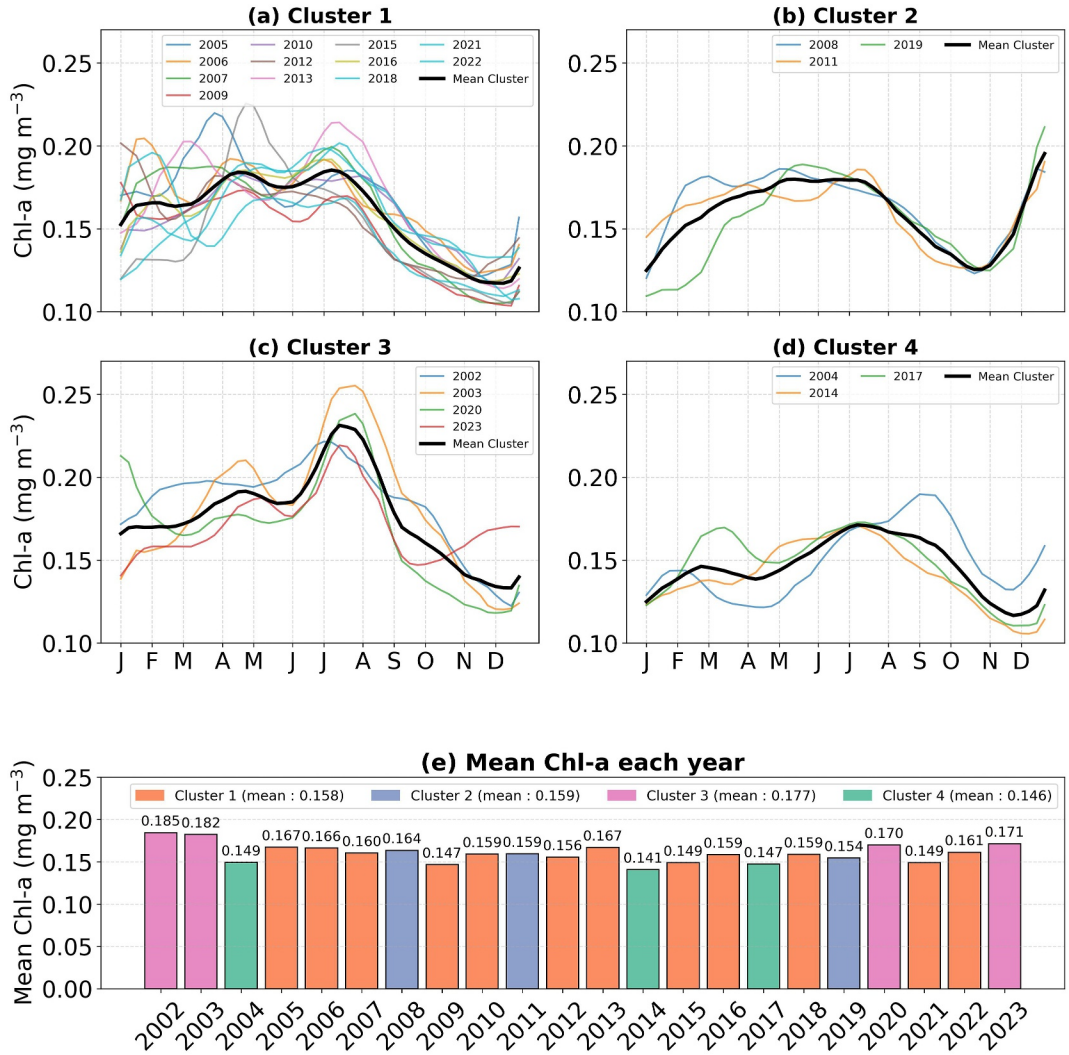

Figure 6. Focus on yearly variability of annual cycles in the MZC. (a–d) present the results of the cluster analysis conducted on annual seasonal cycles of the average Chl-a time serie (in mg m^{-3}) in the MZC. Each year associated to the cluster is represented in a different color. The cluster mean is in bold black. (e) Mean Chl-a concentration in mg m^{-3} are indicated in the histogram.

To disentangle these signals, we separate each calendar year (from 1 January to 31 December) of the spatially averaged time series associated to the NB-MZC phenoregions (from Figure 5c1). Yearly signals from other climatological phenoregions are presented in Figure S5 of Supporting Information S1. We use a k-means algorithm to classify the different years according to their Chl-a shape. The optimal number of clusters, obtained with the method described in Supporting Information S1, is again $k = 4$. Figure 6 shows the repartition of the years for the different clusters in comparison to their mean time series.

The histogram of mean Chl-a each year (Figure 6e) shows a trend similar to the moving average presented in Figure 5c2. There are corresponding local minima in 2004, 2009, 2014, 2017, and 2021.

The first cluster gathers the most of the years (12 years, Figure 6a). The corresponding seasonal cycles vary individually in shape, but all have at least two local maxima, one in winter, peaking around July, and another in late summer or autumn (from March to May). The summer bloom has often a greater amplitude. Chl-a concentration mean value is 0.158 mg m^{-3}.

The second cluster is made of 3 years (2008, 2011, and 2019, Figure 6b). The average seasonal cycle is characterized by a long bloom that increases from January to May. Chl-a concentration mean value is 0.159 mg m^{-3}.

The third cluster gathers 4 years (2002, 2003, 2020, and 2023, Figure 6c). The average seasonal cycle is characterized by a small autumn bloom followed by a strong winter bloom. Chl-a concentration mean corresponds to the highest value with 0.177 mg m^{-3}.

The last cluster regroups 3 years (2004, 2014, and 2017, Figure 6d). The average seasonal cycle is characterized by a long bloom in winter and a smaller one in summer. Chl-a concentration mean is the lower with values of 0.146 mg m^{-3}.

The histogram of mean Chl-a by year (Figure 6e) shows a trend similar to the moving average presented in Figure 5c2. There are corresponding local minimums in 2004, 2009, 2014, 2017, and 2021. Cluster 3 is the most productive, covering two years at the beginning and two years at the end of the studied period. The other clusters alternate for the remaining years. There is a pattern of 2 or 3 years of cluster 1, separated by 1 year of cluster 2 or cluster 4, which suggests a year with a long bloom interspersed with years of smaller blooms.

To conclude, this section examined the interannual variability within each phenoregion with a particular focus on the MZC. The MZC is generally dominated by years exhibiting higher production over the SWIO, relatively evenly distributed over the first 9 months (clusters 1 and 2). However, at the beginning (2002, 2003) and end (2020, 2023) of the time series, larger production events are linked to a more pronounced winter bloom (cluster 3). In contrast, 3 years (2004, 2014, 2017) are characterized by overall weaker production, with both summer and winter blooms reduced (cluster 4). The spatial variations of the phenoregions will be tackled in the following section.

3.4. Spatial Interannual Variability of Phenoregions Distribution

In the previous section, interannual variations have been described within fixed spatial climatological phenoregions. This section presents the temporal variability of shapes and areas of each phenoregion. Applying the method described in Section 2.2, annual map of phenoregions were generated, yielding a total of 22 maps (see Figures S6–S8 in Supporting Information S1). NB and SB phenoregions were separated a posteriori, with the geographical criterion as described in Text S3 of Supporting Information S1. Stable areas are first described (Section 3.4.1), followed by an analysis of interannual variations (Section 3.4.2).

3.4.1. Dominant Regions

From the 22 annual phenoregion maps, while stable long-term general patterns emerge, there is a high variability in their geographical distribution. To analyze the long-term stability, for each pixel, over 22 years, we evaluate which phenoregion is the most recurrent (following the method described by Mayot et al. (2016)). By construction, the map of the dominant interannual phenoregions (Figure 7a) is consistent with the climatological phenoregion map (Figure 4a). The WB forms a band that extends east and north of Madagascar, bordered by the WSB phenoregion. The four characteristic regions of the WSB are found: to the north-east of the domain, a band from Madagascar to Réunion and Mauritius islands, and an area on each side of the MZC. SB-Coasts and SB-SEM also emerge, although the latter is reduced. Finally, for the NB phenoregions, while NB-EM is reduced, NB-MZC is clearly visible.

The degree of membership (DegM) is defined by the number of years in the 22 years in which the most dominant phenoregion is represented, expressed in percentage (Figure 7b). The map of degree of membership shows high spatial variability: some areas are almost always associated with the same phenoregion ($DegM > 90\%$, in yellow in Figure 7b), while others are less stable and often change of membership ($DegM < 25\%$, in dark blue in Figure 7b). This variability is reflected in the dominance map (Figure 7c). The dominance criteria is computed for each pixels, where dominant phenoregions have a degree of membership greater than 50%; it represents areas of stable phenoregions. The WB is almost permanent, with a strong degree of membership ($DegM > 80\%$). The dominant WB area represents 43.82% of the total area, which is similar to the climatological phenoregion. The dominant WSB area is reduced compared to the climatological one, now covering 10.58% of the domain. It has a stable core, especially on the track of cyclonic eddies and dipoles formed in the south of Madagascar (De Ruijter et al., 2005). NB is stable only in the middle of the MZC (5.30% of the total area), in the anticyclonic rings track. NB-EM does not appear on the dominance map, highlighting its low stability. The Madagascar coast appears to be stable for the SB phenoregion, with a coverage close to the climatological phenoregion (the dominant area of the SB-Coasts represents 2.20% of the domain). The SB-SEM phenoregion is almost non-existent, in agreement with

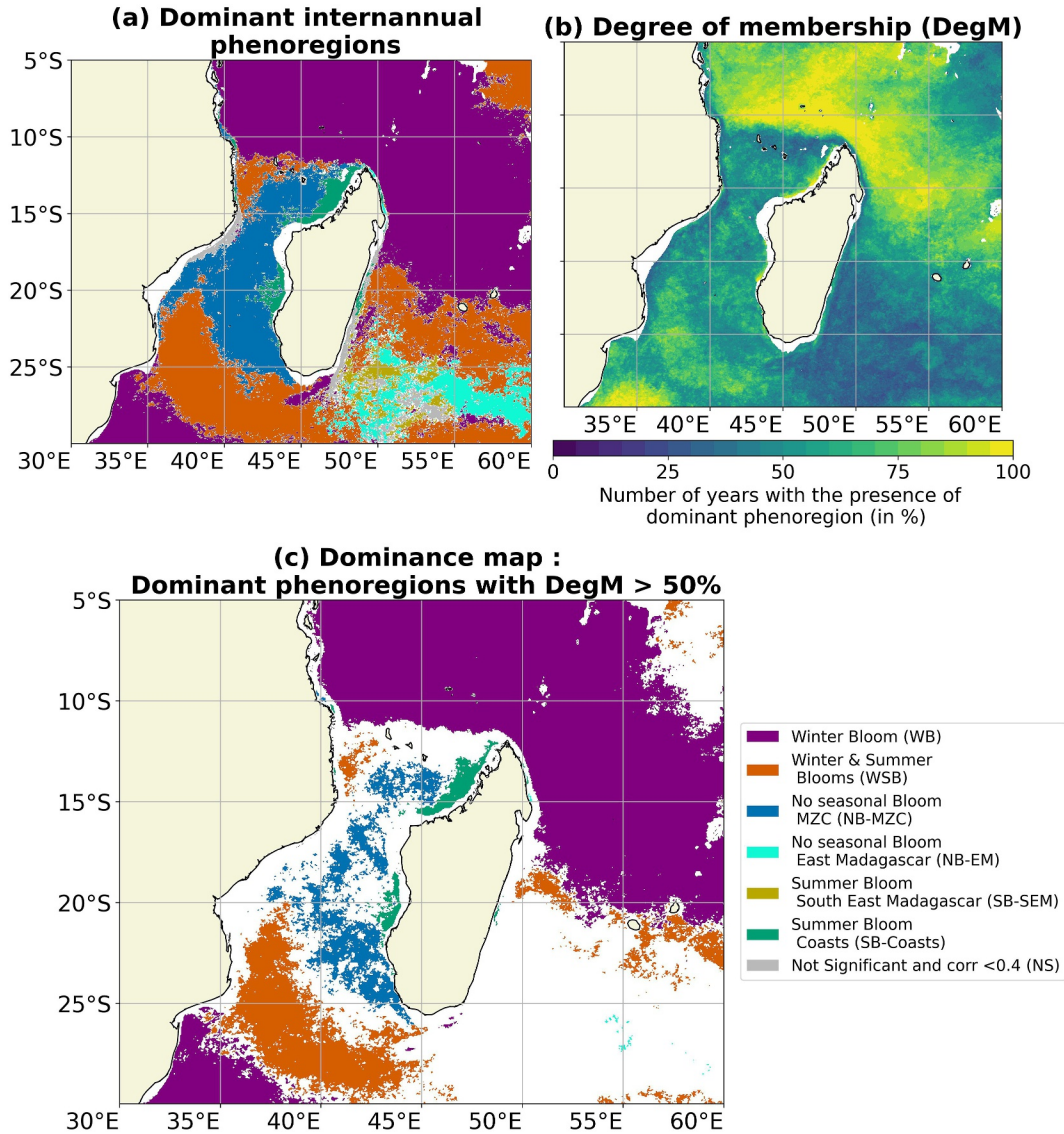

Figure 7. Dominance map. (a) Map of the most recurrent interannual phenoregions for the 22-years period. (b) Map of degree of membership (*DegM*), that is, the number of years with the presence of the dominant phenoregions, in percentage. (c) Map of the dominant interannual phenoregions with $DegM > 50\%$, called the dominance map. Note that NS regions appear in map (a), in gray with an associated *DegM* in panel (b). Those regions are not stable, so they don't appear in panel (c).

the intermittency of the south-east Madagascar bloom (Dilmahamod et al., 2019). SB-SEM and NB-EM do no longer appear in Figure 7c, a posteriori, the separation of the NB and SB regions into sub-regions.

The seasonal cycles of the dominant phenoregions (from Figure 7c) are compared to the seasonal cycles of the climatological phenoregions (in Figure S9 of Supporting Information S1). The two cycles in each phenoregion show the same variation and similar envelopes of variability. This confirms that the centers of these four regions are persistent and their characteristics consistent over time.

3.4.2. Interannual Phenoregions Area Variability

Interannual variations in phenoregion area can reflect changes in the environmental conditions that shape the phenoregions. The evolution of areas is presented in Figure 8. The area fluctuates around the area of the climatological phenoregion except for NB-EM and SB-Coasts which are smaller and bigger, respectively.

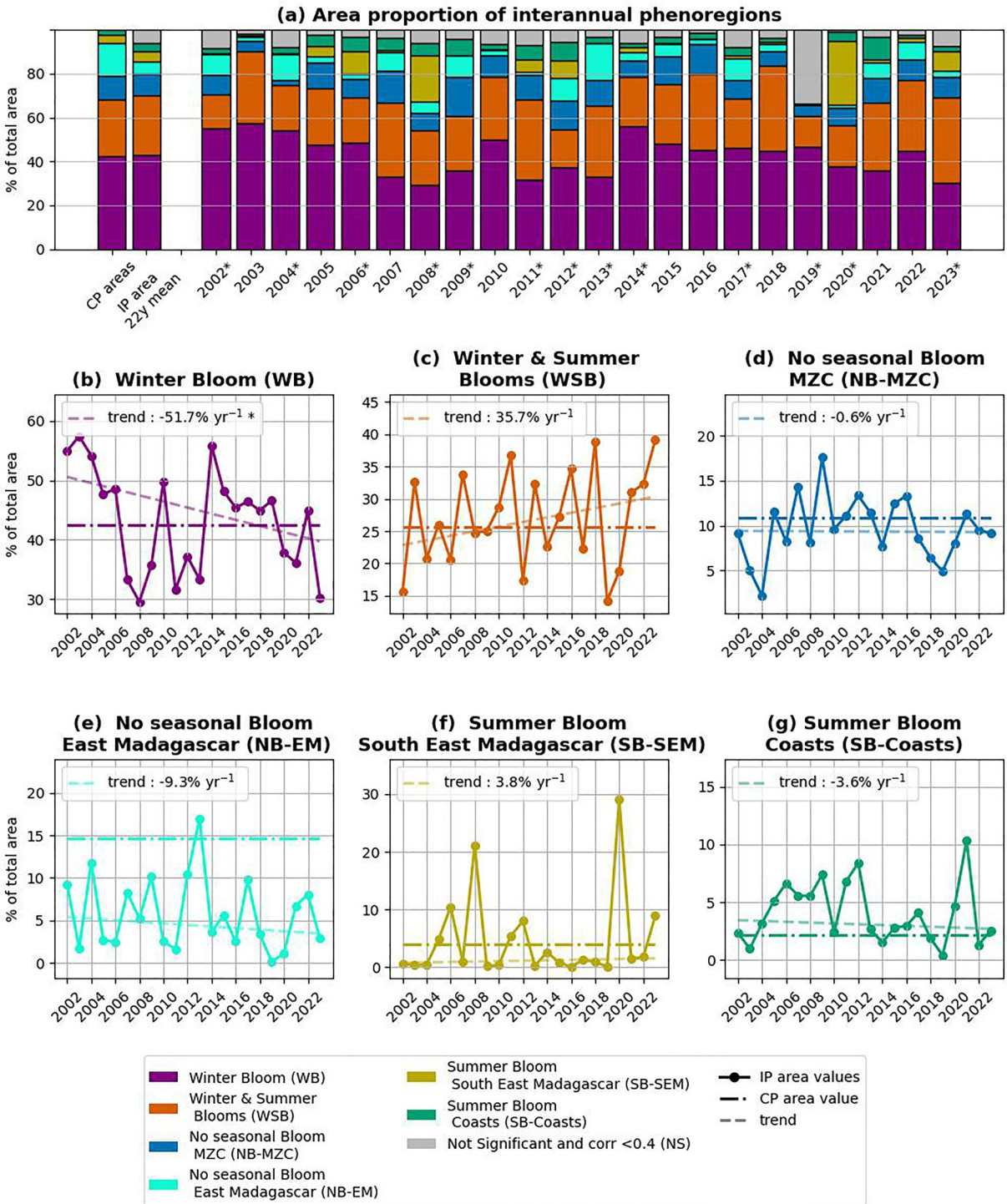

Figure 8. Interannual Phenoregions areas. (a) Area proportion of the interannual phenoregions (in percentage of the total area). Area of climatological phenoregions (CP, from Table 1) are given in first column. 22-year area mean are given in second column. South-east Madagascar blooming years as referenced by Dilmahamod et al. (2019) and Gittings et al. (2024) are indicated with a star. (b–g) Time series of the area covered by the different interannual phenoregions (in percentage of the total area) in dotted line. CP areas are indicated with horizontal dash-dotted line. Trends are shown in dashed line and their equation, calculated with the Theil-Sen method (Akritas et al., 1995), is shown in the legend, with a star (*) indicating trends that are statistically significant at the 90% confidence level.

The WB and WSB are the most expanded phenoregions over the studied years compared to the others. The WB, the larger one, covers between 29% and 57% of the domain. The WB area presents a statistically significant decreasing trend of −51.7% per year (with a 90% confidence level, based on the Theil-Sen method (Akritas et al., 1995)) over 22 years (Figure 8b). Unlike WB, WSB 22-year trend is increasing by a value of 35.7% per year (Figure 8c). As they are adjacent regions, the loss in WB area can be partially explained by a gain in WSB area (as observed in Figures S6–S8 of Supporting Information S1), resulting in opposite decadal trends, that is, an increase in summer blooms compared to winter blooms.

The SB-SEM phenoregion shows a large interannual variability (Figure 8f), with significant spatial expansion events. Indeed, in 2005, 2006, 2008, 2011, 2012, 2020, and 2023, the phenoregion has a greater coverage than the climatological phenoregions. It corresponds to the peaks observed in Figure 5e. During the remaining years, the phenoregion is almost non-existent. In 2019–2020, a massive summer bloom extended over the whole region south of Madagascar (Gittings et al., 2024), explaining the large value observed in 2020 (27% of the SWIO). In 2019, all signals are not significant (30% of the SWIO) due to the particular timing of the bloom, starting 2 months earlier than regular ones.

The SB-Coasts interannual areas are almost always greater than the climatological one (Figure 8g). It is often associated with an expansion of the phenoregion toward different parts of the MZC (Figures S6–S8 in Supporting Information S1). For example, in 2021, the SB-Coasts phenoregion is the most expanded (10% of the SWIO) and completely overlaps the MZC.

The interannual area of the NB-EM phenoregions is almost always smaller than the climatological one (Figure 8e) and ranges from 0% to 16%. The lower values coincide with SB-SEM episodes. In fact, the SB-SEM phenoregion expends over the area characterized as NB-EM in the climatological phenoregions. For example, the NB-EM phenoregion is reduced to almost 0 km^2 in 2020 due to the massive event of this year.

The NB-MZC area varies from 2% to 17% of the SWIO without a clear significant trend (Figure 8d). The smallest NB-MZC interannual phenoregions correspond to the years when the WB, WSB or SB-Coasts phenoregions extend over the MZC (Figures S6–S8 in Supporting Information S1). For example, in 2004, when the NB-MZC covers only 2% of the SWIO, the WB phenoregion extends deep south into the channel. In 2006, 2008 and 2021 it is the SB-Coasts that replaces the NB-MZC. Other local minima, such as in 2010, 2014, and 2018, the northern and southern parts of the WSB phenoregion join in the middle of the channel, then representing entirely the anticyclonic rings corridor. The minimum in 2019 corresponds to the special event mentioned earlier, when a great part of the SWIO is associated to non significant pixels. The observed variations are consistent with the complexity of the processes in the MZC, particularly in the presence of anticyclonic eddies, and reflect the variety of the cycles depicted in Figure 6.

To summarize, phenoregions defined on the climatological seasonal cycles are still found on the interannual scale. Some phenoregions are more stable than others in terms of spatial coverage, underlying various processes at play, which will be discussed later: the WB, core areas of the WSB, SB-Coasts, and the eastern part of the NB-MZC phenoregions define the dominant regions, exhibiting more long-term stability, matching the climatological phenoregions. In contrast, SB-SEM and NB-EM are less stable, with strong interannual variability.

4. Discussion

Using a k-means algorithm on normalized Chl-a climatological seasonal cycles, our analysis revealed six distinct phenoregions in the SWIO, based on their number of blooms and their timing. These regions are consistent with the regionalization previously proposed, at the global scale by Longhurst (1998) and Baudena et al. (2025) and at the regional scale by Lévy et al. (2007) and Riom et al. (2025). Our study provides new insights, on the phenology of the SWIO and especially of the MZC, that was not fully covered by previous studies (Lévy et al., 2007; Longhurst, 1998; Riom et al., 2025). Additionally, we tackled the variability of phenoregions, at temporal and spatial scales, using an up-to-date long-term satellite data set, ensuring the robustness of our results. Our phenoregions are characterized by a stable core area with temporal and spatial interannual variability driven by different processes at play. The processes will be discussed in the following subsections, and summarized in Figure 9.

A limitation of the method is the use of normalized seasonal cycle by the maximum of Chl-a to define the climatological phenoregions. This was necessary to mask the cross-shore concentration gradient. We also needed

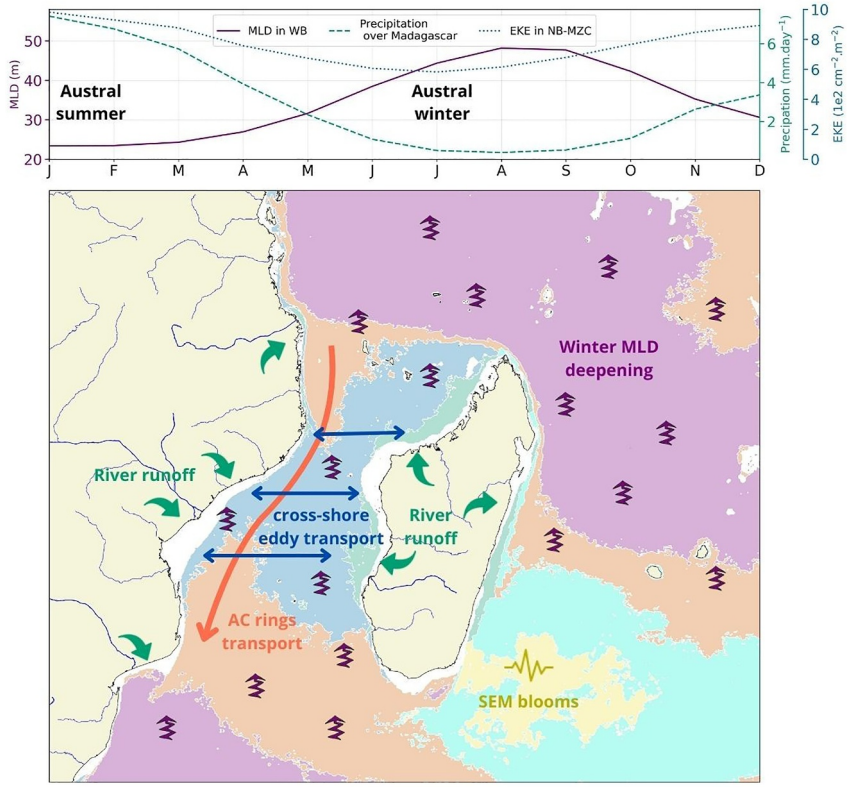

Figure 9. Processes schematic. Presentation of the principal processes likely to shape the phenoregions in the SWIO: in time (upper panel) and space (lower panel). Seasonal cycles of environmental variables are given, averaged over the WB phenoregion for the MLD, over the NB-MZC phenoregion for the EKE and over Madagascar island for precipitations. AC ring pathway is indicated by the orange arrow. Cross-shore horizontal transport by eddies is represented by the blue arrows. River nutrient inputs influence are represented by green arrows. Nutrient enrichment driven by winter MLD deepening is indicated in purple zig-zag arrows. South-east Madagascar Blooms location is in yellow. Data sources are indicated in Availability Statement.

to manually separate the NB and SB phenoregions into two subregions based on SWIO expertise. This choice was motivated by a discernible amplitude difference, attributable to prevailing processes within the respective subregions.

4.1. Winter Processes

In general, the winter bloom is the most significant bloom of the year in most regions of the SWIO, surpassing the summer bloom in terms of Chl-a concentrations (Figure 3). Regions dominated by a winter bloom (i.e., WB and WSB) present a highly marked seasonal cycle (Figure 5 and Table 2), with a bloom starting from April/May and peaking in July/August (Figure 4), representing 65% of the domain. Winter bloom regions are located in the north-east of Madagascar and south of the MZC. The northern part constitutes the northern boundary of the subtropical gyre, known to be oligotrophic (Lamont, Brewin, & Barlow, 2018). In such oligotrophic regions, remineralization is too low to provide all necessary nutrients to fuel phytoplankton production which means that physical processes are key drivers of winter blooms, as suggested by Oglethorpe et al. (2025).

The most well known process leading to a winter bloom is the winter deepening of the mixed layer depth (MLD), likely to occur in the region (Lévy et al., 2007; Longhurst, 1998; Riom et al., 2025). The mixed layer depth averages between 25 and 50 m, with shallower values locally reaching about 15 m in summer and deeper values locally exceeding 100 m in winter (de Boyer Montégut et al., 2004; Schott & McCreary, 2001; see Figure 9 for an example averaged over WB). When the MLD meets the nitracline (which is here in general around 70–80 m, see Riom et al. (2025)), deep nutrient rich waters could be brought up into the photic zone, leading to increased Chl-a production at the surface.

A second possible process is that diapycnal diffusive nitrate fluxes could participate in the mixed layer enrichment, as discussed by Oglethorpe et al. (2025). This could be true along the borders of a subtropical gyre, and here to the west of the Indian Ocean, such as the SWIO.

4.2. Coastal Influence

In contrast to processes leading to a winter bloom, other processes can induce a summer bloom as discussed here. Summer blooms occur in the SWIO (Figure 4) not only near coastal areas (SB-Coasts), but also in offshore regions (WSB and SB-SEM).

On the continental shelf, Chl-a concentrations are higher due to shallow water and riverine inputs (Figure 5). Even if data on the continental shelf were originally discarded due to coastal water type, enriched coastal waters, with high nutrient or Chl-a concentrations, can be advected offshore by currents or eddies, thus expanding beyond the continental shelf (Malauene et al., 2018). The climate of Madagascar is characterized by two seasons (Randriatsara, Hu, Xu, et al., 2022): dry in winter and wet in summer (see the seasonal cycle of precipitations over Madagascar in Figure 9). Numerous rivers concentrated in north-western Madagascar transport summer rainfall to the coast, discharging terrestrial organic matter and nutrients into the SB-Coasts phenoregion, thereby enhancing local Chl-a production.

As the satellite merging algorithms used by OC-CCI are tuned to perform in Case I water (Sathyendranath et al., 2019), we have made the choice to discard Case II waters—coastal data—from our analysis. Sofala Bank, a large and shallow continental shelf along the central Mozambican coast, is therefore excluded from our study. However, this region is under the influence of several rivers, such as the Zambezi, Pungwe, Buzi and Save rivers, which are important sources of nutrient for the MZC (Randriatsara, Hu, Ayugi, et al., 2022). Therefore, it would have been great to access data in this area, but this would imply the use of specific algorithms, tuned to match local in situ observations, or the study of coastal and offshore areas separately, as in the case of Sá et al. (2013).

To the south-east of Madagascar, the summer bloom is a complex and intermittent feature, whose features vary from year to year (Dilmahamod et al., 2019; Longhurst, 2001; Srokosz & Quartly, 2013; Uz, 2007). Longhurst (2001) was the first to link its bloom onset to mixed-layer deepening combined with mesoscale eddy activity. This was also discussed by Srokosz et al. (2004) subsequently. Later studies confirmed the dominant role of turbulent mesoscale circulation in transporting and redistributing nutrients and biomass at the southern tip of Madagascar (Dilmahamod et al., 2020; Huhn et al., 2012; Lévy et al., 2007; Raj et al., 2010; Srokosz & Quartly, 2013; Uz, 2007). Others studies showed that deep MLD is not a systematic prerequisite for bloom development (Dilmahamod et al., 2019; Srokosz & Quartly, 2013; Uz, 2007). Instead, shallow and strongly stratified conditions could favor diazotrophs and facilitate bloom initiation (Uz, 2007).

In situ measurements indicate that south-east Madagascar blooms usually develop in a warm (>26.5°C), shallow mixed layer (30 m; Srokosz and Quartly (2013)) (Dilmahamod et al., 2019) and persist until iron becomes limiting (Srokosz et al., 2015). Interannual variability further modulates bloom expansion: for example, the exceptional 2019–2020 bloom began unusually early, reached much higher levels of Chl-a, and spread farther offshore than other events. Gittings et al. (2024) linked this extreme event to enhanced atmospheric nutrient and iron deposition following severe drought conditions in southern Africa. This event is well characterized in our results (Figure 8): its exceptional spatial extension is clearly seen in Figure S8 (see Supporting Information S1). It extends to the south of the MZC and over all the south-east of Madagascar, which explains why Chl-a concentration outliers are depicted in the WSB and NB-EM phenoregions (Figures 5b and 5d).

Our method has made it possible to define the area of influence of the summer bloom in south-east Madagascar and to study bloom events directly throughout the entire time series in this region. The clustering algorithm has enabled us to track the shape of the bloom from year to year, improving upon the detection method employed by Dilmahamod et al. (2019), which relied on the difference between two boxes in the Indian Ocean.

Compared to winter blooms, summer blooms in the SWIO appear in general more related to external nutrient input, from river runoff that increases during the wet season, or exceptionally from atmospheric deposition.

4.3. MZC: A Complex Region

In this section, the complexity of the MZC, a key part of the SWIO, is discussed. The MZC is a unique area due to its strong mesoscale activity and, particularly, the occurrence of large anticyclonic rings (Halo, Backeberg, et al., 2014; Quartly & Srokosz, 2004).

Our study clearly illustrates the particularity of the channel, which does not have a regular and well shaped seasonal bloom from year to year (Figure 6). There is a relatively higher concentration of Chl-a throughout the year (Figure 4). In this region, mesoscale eddies interact with nutrient-rich coastal waters (Malauene et al., 2014; Quartly & Srokosz, 2004). Coastal waters can be transported offshore by lateral advection through filaments around eddies (Moore et al., 2007; Penven et al., 2025). They can also be trapped in the core of cyclonic eddies (Chenillat et al., 2024; José et al., 2016), fertilizing offshore oligotrophic ocean with nutrient and biological materials (Chenillat et al., 2016). Additionally, several years (Figure 6) display a more pronounced winter bloom, suggesting that winter processes are also at play: MLD deepening may enrich the surface photic layer with deep nutrient-rich water, through the vertical mixing.

The combination of these processes is likely to supply nutrients for the plankton production throughout the year, making Chl-a concentrations oscillating around a base value (0.16 mg m^{-3}, see Figure 4). The interplay between the different processes could explain the variations from year to year.

The summer bloom of the WSB phenoregion may be linked to cross-shore transport of coastal rich waters by eddies, as it is situated in turbulent areas: (a) the north-western portion matches with the anticyclonic rings formation region off Comoros islands (Halo, Backeberg, et al., 2014; Schouten et al., 2003); (b) the band east of Madagascar, near Réunion and Mauritius islands, is an eddy generation area (De Ruijter et al., 2005; Pous et al., 2014); (c) the southern portion of the phenoregion is characterized by the presence of cyclonic eddies and dipoles (De Ruijter et al., 2005), formed by the detachment of the SEMC and propagating westward (Saetre & Da Silva, 1984). This mesoscale activity contributes to the nutrient enrichment by two mechanisms: through local upwelling of deep nutrient-rich waters or through lateral advection of nutrient-rich coastal waters from southern Madagascar (Machu et al., 2002; Ramanantsoa et al., 2018).

The complexity of the MZC is outlined here, with the presence of a strong mesoscale activity (see yearly high level of EKE in the MZC, in Figure 9) that connects nutrient-rich coastal water with offshore region, maintaining year-round Chl-a production around a relatively constant levels.

4.4. Interannual Variability

In terms of interannual variability, regions with a clear winter bloom exhibit high stability. As the MLD is the result of several processes such as surface buoyancy fluxes, stratification or wind forcing, this stability may be a consequence of the large seasonality typical of the Indian Ocean monsoonal variability (Schott & McCreary, 2001). However, climate change is inducing warming in the Indian Ocean, and this excess heat may increase stratification, weaken trade winds and shoal the MLD (Long et al., 2024; Yang et al., 2023; Zhen et al., 2023).

According to the processes discussed earlier, changes in the stratification is likely to lower the area of the WB phenoregion, and tends to increase the area of the WSB phenoregion, as observed in Figure 8b. A shift seems to be observed from a strong single winter bloom to two smaller blooms, one in winter and one in summer. As a consequence, the limit of the WSB off Madagascar is moving northward.

For the summer blooms, there are two different regimes for the two subregions. SB-Coasts is stable because it is related to increased river runoff in the wet season, as discussed in Section 4.2. The rain cycle over Madagascar presents a clear seasonality (Randriatsara, Hu, Ayugi, et al., 2022), and the observed area variations seem to be related to years with higher precipitation. In fact, data from the CHIRPS product v2.0 (Climate Hazards Group InfraRed Precipitation with Station data recommended by Randriatsara, Hu, Xu, et al. (2022)) show that rainfalls over Madagascar have an interannual variability, with higher precipitation between 2003 and 2008, in 2011 and 2020 (Figure S10 in Text S7 of Supporting Information S1). Even if correlation between annual maximum precipitation and SB-Coasts area is not statistically significant, higher precipitation is followed by a greater expansion of the SB-Coasts phenoregion. Summer heavy rains may carry nutrient-rich terrestrial sediments to the sea, allowing an increase in Chl-a (Xu et al., 2020), with a potential lag. However, precipitation over Madagascar

displays also a great spatial variability that needs to be taken into account to explain variations in the spatial extent of SB-Coasts (Ollivier et al., 2023). Further study of hydrological processes is needed to confirm this hypothesis and assess lag between precipitation timing and nutrient arrival to the ocean.

For the MZC phenoregions (NB-MZC and WSB), stable areas seem to coincide with the region of high occurrence of cyclonic eddies, in the eastern and southern parts of the channel (Halo, Backeberg, et al., 2014).

The SWIO dynamical complexity involves several different processes. While the region may be influenced by climate modes such as El Niño (Reason et al., 2000) and the Indian Ocean Dipole (Currie et al., 2013; Palastanga et al., 2006), distinguishing their relative contributions remains challenging (De Ruijter et al., 2005). The correlations between climate indices and Chl-a or area variations were tested but only limited significant relationships emerged.

5. Conclusion

A 22-year time series of satellite ocean color was used to study the seasonal cycles of Chl-a in the SWIO. Our analysis led to the definition of six climatological phenoregions, differentiated by bloom phenology.

Winter bloom dominates in most of the SWIO. It should be related to MLD deepening, which generates vertical transport of nutrients toward the photic zone, enabling increase in Chl-a. As MLD deepening is driven by seasonal wind and buoyancy fluxes, the winter bloom remains stable over years, resulting in stable WB and WSB phenoregions. Other regions of the SWIO are characterized by summer blooms, either a single one (SB phenoregions) or a secondary one (for the WSB phenoregion). They may often be associated with an increase in terrestrial nutrient inputs from rivers during the wet season. The south-east Madagascar summer bloom is also well delineated by the clustering at spatial and interannual scales. Finally, the MZC is characterized by a low seasonality in Chl-a but with relatively higher concentrations of Chl-a throughout the year. This may be due to constant nutrient supply to offshore waters by eddy transport.

Some limitations of the method can be highlighted. First, normalization by the maximum value of the seasonal cycle was necessary to minimize the dominance of the cross-shore concentration gradient, thereby allowing to focus on bloom timing. As a result, some phenoregions grouped areas with similar Chl-a seasonal patterns but substantially different absolute concentration levels; such regions were separated a posteriori to ensure a more accurate description of SWIO bloom phenology and underlying processes. Second, the use of satellite OC-CCI data required excluding coastal areas to focus exclusively on Case I waters. Inclusion of coastal waters would have been valuable for assessing the influence of riverine nutrient inputs.

This analysis allowed separation and characterization of contrasting phenoregions, opening avenues for investigating the processes driving these differences. We propose applying this method to numerical model simulations in a future, similarly to Koné et al. (2009) work. This would provide complete spatial and temporal coverage of the domain, including the coast and the water column, without spatio-temporal gaps. It would also give access to comprehensive variables, fluxes and budgets to elucidate the processes underlying phenoregion separation. The method could also be applied on other variables than Chl-a, as Huot et al. (2019) proposed on the Indian Ocean scale.

In summary, characterizing the seasonality of Chl-a in the SWIO provides insights into regional marine ecosystems and their sensitivity to environmental variability. Identifying the timing and amplitude of phytoplankton seasonal cycles enhances understanding the dynamics of the trophic web base. This knowledge is critical for anticipating ecosystem responses to climate-driven changes, and for supporting sustainable fisheries management and marine protected areas conservation (Malauene et al., 2024).

Acronyms

Chl-a	Chlorophyll-a
CHIRPS	Climate Hazards Group InfraRed Precipitation with Station
CMEMS	Copernicus Marine Environmental Monitoring Service
CP	Climatological Phenoregions

EAFR	Eastern Africa Coastal Province
EKE	Eddy Kinetic Energy
ENSO	El Niño Southern Oscillation
ESA	European Space Agency
IOD	Indian Ocean Dipole
IP	Interannual Phenoregions
ISSG	Indian South Subtropical Gyre Province
MEI	Multivariate ENSO Index
MLD	Mixed Layer Depth
MONS	Indian Monsoon Gyre Province
MZC	Mozambique Channel
NB	No seasonal Bloom Phenoregion
NB-EM	No seasonal Bloom Phenoregion, Eastern Madagascar
NB-MZC	No seasonal Bloom Phenoregion, in the Mozambique Channel
NEMC	North East Madagascar Current
NOAA	National Oceanic and Atmospheric Administration
NS	No Significant
OC-CCI	Ocean Color-Climate Change Initiative
SB	Summer Bloom phenoregion
SB-Coasts	Summer Bloom phenoregion, at the Coasts
SB-SEM	Summer Bloom phenoregion, at the South-East of Madagascar
SEC	South Equatorial Current
SEMC	South-East Madagascar Current
SICC	South Indian Counter Current
SWIO	South-West Indian Ocean
WB	Winter Bloom phenoregion
WSB	Winter & Summer Blooms phenoregion

Inclusion in Global Research Statement

This study was conducted through a collaborative research partnership between institutions in France and Mozambique, including public and private organizations. All co-authors met the AGU authorship criteria, contributing substantially to the conception, analysis, interpretation, and writing of the manuscript. Local collaborators from Mozambique were engaged in contextualization of results, and manuscript preparation, ensuring that regional knowledge and expertise were incorporated. This collaborative framework reflects our commitment to equitable research practices and the principles outlined in the TRUST Code, promoting transparency, inclusion, and recognition of local contributions in international research.

Conflict of Interest

The authors declare no conflicts of interest relevant to this study.

Availability Statement

Satellite observations presented here are distributed by ESA Ocean Colour-Climate Change Initiative for Chlorophyll-a (https://doi.org/10.24381/cds.f85b319d), and by Copernicus Marine Service for Mixed Layer Depth (Mulet et al., 2012), Sea Surface Height (https://doi.org/10.48670/moi-00148). Climate Indexes such as Multivariate ENSO Index and the Indian Ocean Dipole are available on NOAA website (https://www.psl.noaa.gov/enso/mei and https://psl.noaa.gov/data/timeseries/month/DMI/). MLD was acquired from the Copernicus Marine Environmental Monitoring Service (CMEMS) "Multi Observation Global Ocean 3D Temperature Salinity Height Geostrophic Current" product (https://doi.org/10.48670/moi-00052, available online at http://marine.copernicus.eu), using the *mlotst* variable (Mulet et al., 2012). Rainfall data on Madagascar island was extracted from CHIRPS (Climate Hazards Group InfraRed Precipitation with Station data) product v2.0, as *precip* variable (Funk et al. (2014), available online at https://data.chc.ucsb.edu/products). EKE was calculated from u and v, the zonal and meridional current component respectively, derived from Sea Surface Height (SSH; in m). SSH was acquired from CMEMS "Global Ocean Gridded L4 Sea Surface Heights And Derived Variables Reprocessed 1993 Ongoing" product, as *ssh* variable (https://doi.org/10.48670/moi-00148).

Acknowledgments
We thank the Belmont Forum for initiating the research theme within the framework of the Ocean Front Change project. We also acknowledge financial and logistical support from Actimar and the Université de Bretagne Occidentale (UBO). This work has received government funding managed by the French National Research Agency under France 2030, reference ANR-22-EXBR-0004 and ANR-24-EPAR-0004-03. We are grateful to all colleagues and collaborators who contributed to data processing, analysis, and discussions that improved this study. We acknowledge suggestions of all reviewers that contributed to improving the paper substantially.

References

Akritas, M. G., Murphy, S. A., & LaValley, M. P. (1995). The Theil-Sen estimator with doubly censored data and applications to astronomy. *Journal of the American Statistical Association*, *90*(429), 170–177. https://doi.org/10.1080/01621459.1995.10476499

Barlow, R., Lamont, T., Morris, T., Sessions, H., & van den Berg, M. (2014). Adaptation of phytoplankton communities to mesoscale eddies in the Mozambique Channel. *Deep-Sea Research Part II Topical Studies in Oceanography*, *100*, 106–118. https://doi.org/10.1016/j.dsr2.2013.10.020

Baudena, A., Riom, W., Taillandier, V., Mayot, N., Mignot, A., & D'Ortenzio, F. (2025). Comparing satellite and BGC-Argo chlorophyll estimation: A phenological study. *Remote Sensing of Environment*, *326*, 114743. https://doi.org/10.1016/j.rse.2025.114743

Bristow, L. A., Mohr, W., Ahmerkamp, S., & Kuypers, M. M. M. (2017). Current biology nutrients that limit growth in the ocean. *Current Biology*, *27*(11), 474–478. https://doi.org/10.1016/j.cub.2017.03.030

Carr, M. D., Aguiar-González, B., Hermes, J., Veitch, J., & Reason, C. (2025). The role of Rossby waves and Indonesian throughflow waters in shaping the phytoplankton bloom over the Seychelles Chagos thermocline ridge: A biogeochemical Argo case study. *Journal of Geophysical Research: Oceans*, *130*(10), e2025JC022742. https://doi.org/10.1029/2025JC022742

Chelton, D. B., Schlax, M. G., & Samelson, R. M. (2011). Global observations of nonlinear mesoscale eddies. *Progress in Oceanography*, *91*(2), 167–216. https://doi.org/10.1016/j.pocean.2011.01.002

Chenillat, F., Deshaies, E., Arens, A., & Penven, P. (2024). Role of mesoscale eddies in the biogeochemistry of the Mozambique Channel. *Frontiers in Marine Science*, *11*, 1402776. https://doi.org/10.3389/fmars.2024.1402776

Chenillat, F., Franks, P. J., & Combes, V. (2016). Biogeochemical properties of eddies in the California current system. *Geophysical Research Letters*, *43*(11), 5812–5820. https://doi.org/10.1002/2016GL068945

Coleman, D. C., Crossley, D., & Hendrix, P. F. (2004). Primary production processes in soils: Roots and rhizosphere associates. *Fundamentals of Soil Ecology*, 23–46. https://doi.org/10.1016/B978-012179726-3/50003-4

Collins, C., Hermes, J. C., Roman, R. E., & Reason, C. J. (2016). First dedicated hydrographic survey of the Comoros basin. *Journal of Geophysical Research: Oceans*, *121*(2), 1291–1305. https://doi.org/10.1002/2015JC011418

Cossa, O., Pous, S., Penven, P., Capet, X., & Reason, C. J. (2016). Modelling cyclonic eddies in the Delagoa Bight region. *Continental Shelf Research*, *119*, 14–29. https://doi.org/10.1016/j.csr.2016.03.006

Currie, J. C., Lengaigne, M., Vialard, J., Kaplan, D. M., Aumont, O., Naqvi, S. W., & Maury, O. (2013). Indian Ocean dipole and El Niño/southern oscillation impacts on regional chlorophyll anomalies in the Indian Ocean. *Biogeosciences*, *10*, 6677–6698. https://doi.org/10.5194/bg-10-6677-2013

Dai, M., Luo, Y. W., Achterberg, E. P., Browning, T. J., Cai, Y., Cao, Z., et al. (2023). Upper ocean biogeochemistry of the oligotrophic North Pacific Subtropical Gyre: From nutrient sources to carbon export. *Reviews of Geophysics*, *61*(3), e2022RG000800. https://doi.org/10.1029/2022RG000800

de Boyer Montégut, C., Madec, G., Fischer, A. S., Lazar, A., & Iudicone, D. (2004). Mixed layer depth over the global ocean: An examination of profile data and a profile-based climatology. *Journal of Geophysical Research*, *109*(C12), 1–20. https://doi.org/10.1029/2004JC002378

De Falco, C., Desbiolles, F., Bracco, A., & Pasquero, C. (2022). Island mass effect: A review of oceanic physical processes. *Frontiers in Marine Science*, *9*, 894860. https://doi.org/10.3389/fmars.2022.894860

Derrick, T. R., Bates, B. T., & Dufek, J. S. (1993). Evaluation of time series data sets using the Pearson product-moment correlation coefficient. *Medicine and science in sports and exercise*, *26*(7), 919–928.

De Ruijter, W. P., Ridderinkhof, H., & Schouten, M. W. (2005). Variability of the southwest Indian Ocean. *Philosophical Transactions of the Royal Society A: Mathematical, Physical and Engineering Sciences*, *363*(1826), 63–76. https://doi.org/10.1098/rsta.2004.1478

Dilmahamod, A. F., Hermes, J. C., & Reason, C. J. (2016). Chlorophyll-a variability in the Seychelles-Chagos thermocline ridge: Analysis of a coupled biophysical model. *Journal of Marine Systems*, *154*, 220–232. https://doi.org/10.1016/j.jmarsys.2015.10.011

Dilmahamod, A. F., Penven, P., Aguiar-González, B., Reason, C. J., & Hermes, J. C. (2019). A new definition of the South-East Madagascar bloom and analysis of its variability. *Journal of Geophysical Research: Oceans*, *124*(3), 1717–1735. https://doi.org/10.1029/2018JC014582

Dilmahamod, A. F., Penven, P., Aguiar-González, B., Reason, C. J., & Hermes, J. C. (2020). A model investigation of the influences of the South-East Madagascar current on the South-East Madagascar bloom. *Journal of Geophysical Research: Oceans*, *125*(6), e2019JC015761. https://doi.org/10.1029/2019JC015761

D'Ortenzio, F., & Dalcaì, M. R. (2009). On the trophic regimes of the Mediterranean Sea: A satellite analysis. *Tech. Rep.*, *6*. https://doi.org/10.5194/bg-6-139-2009

Fendereski, F., Vogt, M., Payne, M. R., Lachkar, Z., Gruber, N., Salmanmahiny, A., & Hosseini, S. A. (2014). Biogeographic classification of the Caspian Sea. *Biogeosciences*, *11*(22), 6451–6470. https://doi.org/10.5194/bg-11-6451-2014

Ferreira, A., Brotas, V., Palma, C., Borges, C., & Brito, A. C. (2021). Assessing phytoplankton bloom phenology in upwelling-influenced regions using ocean color remote sensing. *Remote Sensing*, *13*(4), 1–27. https://doi.org/10.3390/rs13040675

Funk, C. C., Peterson, P. J., Landsfeld, M. F., Pedreros, D. H., Verdin, J. P., Rowland, J. D., et al. (2014). A quasi-global precipitation time series for drought monitoring: U.S. geological survey data series (Technical Report). https://doi.org/10.3133/ds832

Gittings, J. A., Dall'Olmo, G., Tang, W., Llort, J., Jebri, F., Livanou, E., et al. (2024). An exceptional phytoplankton bloom in the southeast Madagascar sea driven by African dust deposition. *PNAS Nexus*, *3*(10), 386. https://doi.org/10.1093/pnasnexus/pgae386

Halo, I., Backeberg, B., Penven, P., Ansorge, I., Reason, C., & Ullgren, J. E. (2014). Eddy properties in the Mozambique Channel: A comparison between observations and two numerical ocean circulation models. *Deep-Sea Research Part II Topical Studies in Oceanography*, *100*, 38–53. https://doi.org/10.1016/j.dsr2.2013.10.015

Halo, I., Penven, P., Backeberg, B., Ansorge, I., Shillington, F., & Roman, R. (2014). Mesoscale eddy variability in the southern extension of the East Madagascar Current: Seasonal cycle, energy conversion terms, and eddy mean properties. *Journal of Geophysical Research: Oceans*, *119*(10), 2014JC009820. https://doi.org/10.1002/2014jc009820

Hammond, M. L., Beaulieu, C., Henson, S. A., & Sahu, S. K. (2018). Assessing the presence of discontinuities in the ocean color satellite record and their effects on chlorophyll trends and their uncertainties. *Geophysical Research Letters*, *45*(15), 7654–7662. https://doi.org/10.1029/2017GL076928

Huhn, F., Kameke, A. V., Pérez-Muñuzuri, V., Olascoaga, M. J., & Beron-Vera, F. J. (2012). The impact of advective transport by the south Indian Ocean countercurrent on the Madagascar plankton bloom. *Geophysical Research Letters*, *39*. https://doi.org/10.1029/2012GL051246

Huot, Y., Antoine, D., & Daudon, C. (2019). Partitioning the Indian Ocean based on surface fields of physical and biological properties. *Deep-Sea Research Part II Topical Studies in Oceanography*, *166*, 75–89. https://doi.org/10.1016/j.dsr2.2019.04.002

José, Y. S., Aumont, O., Machu, E., Penven, P., Moloney, C. L., & Maury, O. (2014). Influence of mesoscale eddies on biological production in the Mozambique Channel: Several contrasted examples from a coupled ocean-biogeochemistry model. *Deep-Sea Research Part II Topical Studies in Oceanography*, *100*, 79–93. https://doi.org/10.1016/j.dsr2.2013.10.018

José, Y. S., Penven, P., Aumont, O., Machu, E., Moloney, C. L., Shillington, F., & Maury, O. (2016). Suppressing and enhancing effects of mesoscale dynamics on biological production in the Mozambique Channel. *Journal of Marine Systems*, *158*, 129–139. https://doi.org/10.1016/j.jmarsys.2016.02.003

Koné, V., Aumont, O., Lévy, M., & Resplandy, L. (2009). Physical and biogeochemical controls of the phytoplankton seasonal cycle in the Indian Ocean: A modeling study. *Geophysical Monograph Series*, *185*, 147–166. https://doi.org/10.1029/2008GM000700

Krug, L. A., Platt, T., Sathyendranath, S., & Barbosa, A. B. (2018). Patterns and drivers of phytoplankton phenology off SW Iberia: A phenoregion based perspective. *Progress in Oceanography*, *165*, 233–256. https://doi.org/10.1016/j.pocean.2018.06.010

Lamont, T., Barlow, R. G., & Brewin, R. J. (2018). Variations in remotely-sensed phytoplankton size structure of a cyclonic eddy in the southwest Indian Ocean. *Remote Sensing*, *10*(7), 1143. https://doi.org/10.3390/rs10071143

Lamont, T., Brewin, R. J., & Barlow, R. G. (2018). Seasonal variation in remotely-sensed phytoplankton size structure around southern Africa. *Remote Sensing of Environment*, *204*, 617–631. https://doi.org/10.1016/j.rse.2017.09.038

Lamont, T., Roberts, M. J., Barlow, R. G., Morris, T., & van den Berg, M. A. (2010). Circulation patterns in the Delagoa Bight, Mozambique, and the influence of deep ocean eddies. *African Journal of Marine Science*, *32*(3), 553–562. https://doi.org/10.2989/1814232X.2010.538147

Le Borgne, R., Matear, R., Allain, V., & Shane, G. (2011). In J. D. Bell, J. E. Johnson, & A. J. Hobday (Eds.), *Vulnerability of open ocean food webs in the tropical Pacific to climate change* (Technical Report).

Lee, Z. P., & Hu, C. (2006). Global distribution of case-1 waters: An analysis from SeaWiFS measurements. *Remote Sensing of Environment*, *101*(2), 270–276. https://doi.org/10.1016/j.rse.2005.11.008

Lévy, M., André, J.-M., Shankar, D., Durand, F., & Shenoi, S. S. C. (2006). A quantitative method for describing the seasonal cycles of surface chlorophyll in the Indian Ocean. In *Remote sensing of the marine environment* (Vol. 6406, p. 640611). SPIE. https://doi.org/10.1117/12.693587

Lévy, M., Shankar, D., André, J. M., Shenoi, S. S., Durand, F., & de Boyer Montégut, C. (2007). Basin-wide seasonal evolution of the Indian Ocean's phytoplankton blooms. *Journal of Geophysical Research*, *112*(C12). https://doi.org/10.1029/2007JC004090

Long, S. M., Zhao, S., Gao, Z., Sun, S., Shi, J. R., Ying, J., et al. (2024). Weakened seasonality of the ocean surface mixed layer depth in the southern Indian Ocean during 1980–2019. *Geophysical Research Letters*, *51*(7), e2023GL107644. https://doi.org/10.1029/2023GL107644

Longhurst, A. (1998). *Ecological geography of the sea*. Elsevier. https://doi.org/10.1016/B978-0-12-455521-1.X5000-1

Longhurst, A. (2001). A major seasonal phytoplankton bloom in the Madagascar basin. *Deep-Sea Research I*, *48*(11), 2413–2422. https://doi.org/10.1016/s0967-0637(01)00024-3

Lutjeharms, J. (2006). The Agulhas Current retroflection. In *The Agulhas current* (pp. 151–207). Springer Berlin Heidelberg. https://doi.org/10.1007/3-540-37212-1_6

Machu, E., Lutjeharms, J. R., Webb, A. M., & Aken, H. M. V. (2002). First hydrographic evidence of the southeast Madagascar upwelling cell. *Geophysical Research Letters*, *29*(21), 5-1-5–4. https://doi.org/10.1029/2002GL015381

Malauene, B. S., Lett, C., Marsac, F., Penven, P., Abdula, S., Moloney, C. L., & Roberts, M. J. (2024). Influence of Mozambique Channel eddies on larval loss of two shallow-water commercial shrimp species. *PLOS Climate*, *3*(6), e0000414. https://doi.org/10.1371/journal.pclm.0000414

Malauene, B. S., Moloney, C. L., Lett, C., Roberts, M. J., Marsac, F., & Penven, P. (2018). Impact of offshore eddies on shelf circulation and river plumes of the Sofala Bank, Mozambique Channel. *Journal of Marine Systems*, *185*, 1–12. https://doi.org/10.1016/j.jmarsys.2018.05.001

Malauene, B. S., Shillington, F. A., Roberts, M. J., & Moloney, C. L. (2014). Cool, elevated chlorophyll-a waters off northern Mozambique. *Deep-Sea Research Part II Topical Studies in Oceanography*, *100*, 68–78. https://doi.org/10.1016/j.dsr2.2013.10.017

Matsushita, B., Yang, W., Chang, P., Yang, F., & Fukushima, T. (2012). A simple method for distinguishing global case-1 and case-2 waters using SeaWiFS measurements. *ISPRS Journal of Photogrammetry and Remote Sensing*, *69*, 74–87. https://doi.org/10.1016/j.isprsjprs.2012.02.008

Mayot, N., D'Ortenzio, F., D'Alcalà, M. R., Lavigne, H., & Claustre, H. (2016). Interannual variability of the Mediterranean trophic regimes from ocean color satellites. *Biogeosciences*, *13*(6), 1901–1917. https://doi.org/10.5194/bg-13-1901-2016

Mélin, F., Vantrepotte, V., Chuprin, A., Grant, M., Jackson, T., & Sathyendranath, S. (2017). Assessing the fitness-for-purpose of satellite multi-mission ocean color climate data records: A protocol applied to OC-CCI chlorophyll-a data. *Remote Sensing of Environment*, *203*, 139–151. https://doi.org/10.1016/j.rse.2017.03.039

Messié, M., Petrenko, A., Doglioli, A. M., Aldebert, C., Martinez, E., Koenig, G., et al. (2020). The delayed island mass effect: How islands can remotely trigger blooms in the oligotrophic ocean. *Geophysical Research Letters*, *47*(2), e2019GL085282. https://doi.org/10.1029/2019GL085282

Moore, T. S., Matear, R. J., Marra, J., & Clementson, L. (2007). Phytoplankton variability off the western Australian coast: Mesoscale eddies and their role in cross-shelf exchange. *Deep-Sea Research Part II Topical Studies in Oceanography*, *54*(8–10), 943–960. https://doi.org/10.1016/j.dsr2.2007.02.006

Morel, A. (1988). Optical modeling of the upper ocean in relation to its biogenous matter content (case I waters). *Journal of Geophysical Research*, *93*(C9), 10749–10768. https://doi.org/10.1029/jc093ic09p10749

Mulet, S., Rio, M. H., Mignot, A., Guinehut, S., & Morrow, R. (2012). A new estimate of the global 3D geostrophic ocean circulation based on satellite data and in-situ measurements. *Deep-Sea Research Part II Topical Studies in Oceanography*, *77–80*, 70–81. https://doi.org/10.1016/j.dsr2.2012.04.012

Nehama, F. P. J., & Reason, C. J. (2015). Modelling the Zambezi River plume. *African Journal of Marine Science*, *37*(4), 593–604. https://doi.org/10.2989/1814232X.2015.1113202

Nehama, F. P. J., & Reason, C. J. C. (2014). Morphology of the Zambezi River plume on the Sofala bank, Mozambique. *Western Indian Ocean Journal of Marine Science*, *13*, 1–10.

Nicholson, S.-A., Ryan-Keogh, T. J., Thomalla, S. J., Chang, N., & Smith, M. E. (2025). Observed global ocean phytoplankton phenology indices. *Earth System Science Data*, *17*, 1959–1975. https://doi.org/10.5281/zenodo.8402932

Oglethorpe, K., Fernández Castro, B., Spingys, C. P., Naveira Garabato, A. C., & Williams, R. G. (2025). The role of mesoscale eddy stirring and microscale turbulence in sustaining biological production in the subtropical gyres. *Global Biogeochemical Cycles*, *39*(9), e2024GB008180. https://doi.org/10.1029/2024GB008180

Ollivier, C. C., Carrière, S. D., Heath, T., Olioso, A., Rabefitia, Z., Rakoto, H., et al. (2023). Ensemble precipitation estimates based on an assessment of 21 gridded precipitation datasets to improve precipitation estimations across Madagascar. *Journal of Hydrology: Regional Studies*, *47*, 101400. https://doi.org/10.1016/j.ejrh.2023.101400

Palastanga, V., van Leeuwen, P. J., & de Ruijter, W. P. (2006). A link between low-frequency mesoscale eddy variability around Madagascar and the large-scale Indian Ocean variability. *Journal of Geophysical Research*, *111*(C9). https://doi.org/10.1029/2005JC003081

Penven, P., Halo, I., Pous, S., & Marié, L. (2014). Cyclogeostrophic balance in the Mozambique Channel. *Journal of Geophysical Research: Oceans*, *119*(2), 1054–1067. https://doi.org/10.1002/2013JC009528

Penven, P., Ternon, J. F., Noyon, M., Herbette, S., Cambon, G., Comby, C., et al. (2025). Characterizing the central structure of a mesoscale eddy-ring dipole in the Mozambique Channel from in situ observations. *Journal of Geophysical Research: Oceans*, *130*(3), e2024JC021913. https://doi.org/10.1029/2024JC021913

Pous, S., Lazure, P., André, G., Dumas, F., Halo, I., & Penven, P. (2014). Circulation around la Réunion and Mauritius islands in the south-western Indian Ocean: A modeling perspective. *Journal of Geophysical Research: Oceans*, *119*(3), 1957–1976. https://doi.org/10.1002/2013JC009704

Quartly, G. D., & Srokosz, M. A. (2004). Eddies in the southern Mozambique Channel. *Deep-Sea Research Part II Topical Studies in Oceanography*, *51*(1–3), 69–83. https://doi.org/10.1016/j.dsr2.2003.03.001

Raapoto, H., Martinez, E., Petrenko, A., Doglioli, A., Gorgues, T., Sauzède, R., et al. (2019). Role of iron in the Marquesas island mass effect. *Journal of Geophysical Research: Oceans*, *124*(11), 7781–7796. https://doi.org/10.1029/2019JC015275

Racault, M. F., Le Quéré, C., Buitenhuis, E., Sathyendranath, S., & Platt, T. (2012). Phytoplankton phenology in the global ocean. *Ecological Indicators*, *14*(1), 152–163. https://doi.org/10.1016/j.ecolind.2011.07.010

Raj, R. P., Peter, B. N., & Pushpadas, D. (2010). Oceanic and atmospheric influences on the variability of phytoplankton bloom in the south-western Indian Ocean. *Journal of Marine Systems*, *82*(4), 217–229. https://doi.org/10.1016/j.jmarsys.2010.05.009

Ramanantsoa, J. D., Krug, M., Penven, P., Rouault, M., & Gula, J. (2018). Coastal upwelling south of Madagascar: Temporal and spatial variability. *Journal of Marine Systems*, *178*, 29–37. https://doi.org/10.1016/j.jmarsys.2017.10.005

Randriatsara, H. H. R. H., Hu, Z., Ayugi, B., Makula, E. K., Vuguziga, F., & Nkunzimana, A. (2022). Interannual characteristics of rainfall over Madagascar and its relationship with the Indian Ocean Sea surface temperature variation. *Theoretical and Applied Climatology*, *148*(1–2), 349–362. https://doi.org/10.1007/s00704-022-03950-8

Randriatsara, H. H. R. H., Hu, Z., Xu, X., Ayugi, B., Sian, K. T. C. L. K., Mumo, R., & Ongoma, V. (2022). Evaluation of gridded precipitation datasets over Madagascar. *International Journal of Climatology*, *42*(13), 7028–7046. https://doi.org/10.1002/joc.7628

Reason, C. J., Allan, R. J., Lindesay, J. A., & Ansell, T. J. (2000). Enso and climatic signals across the Indian Ocean basin in the global context: Part I, interannual composite patterns. *International Journal of Climatology*, *20*, 1285–1327. https://doi.org/10.1002/1097-0088(200009)20:11⟨1285::AID-JOC536⟩3.0.CO;2-R

Riom, W., Taillandier, V., Dimier, C., D'Ortenzio, F., & Claustre, H. (2025). Biogeochemical float deployment strategy in the southwestern Indian Ocean. *Deep-Sea Research Part II Topical Studies in Oceanography*, *222*, 105504. https://doi.org/10.1016/j.dsr2.2025.105504

Sá, C., Leal, M. C., Silva, A., Nordez, S., André, E., Paula, J., & Brotas, V. (2013). Variation of phytoplankton assemblages along the Mozambique coast as revealed by HPLC and microscopy. *Journal of Sea Research*, *79*, 1–11. https://doi.org/10.1016/j.seares.2013.01.001

Saetre, R., & Da Silva, A. J. (1984). The circulation of the Mozambique Channel. *Deep-Sea Research, Part A: Oceanographic Research Papers*, *31*(5), 485–508. https://doi.org/10.1016/0198-0149(84)90098-0

Sathyendranath, S., Brewin, R. J., Brockmann, C., Brotas, V., Calton, B., Chuprin, A., et al. (2019). An ocean-colour time series for use in climate studies: The experience of the ocean-colour climate change initiative (OC-CCI). *Sensors*, *19*, 4285. https://doi.org/10.3390/s19194285

Schott, F. A., & McCreary, J. P. (2001). The monsoon circulation of the Indian Ocean. *Progress in Oceanography*, *51*(1), 1–123. https://doi.org/10.1016/S0079-6611(01)00083-0

Schott, F. A., Xie, S. P., & McCreary, J. P. (2009). Indian Ocean circulation and climate variability. *Reviews of Geophysics*, *47*(1). https://doi.org/10.1029/2007RG000245

Schouten, M. W., De Ruijter, W. P., Leeuwen, P. J. V., & Ridderinkhof, H. (2003). Eddies and variability in the Mozambique Channel. *Deep-Sea Research Part II Topical Studies in Oceanography*, *50*(12–13), 1987–2003. https://doi.org/10.1016/S0967-0645(03)00042-0

Schouten, M. W., de Ruijter, W. P., van Leeuwen, P. J., & Dijkstra, H. A. (2002). An oceanic teleconnection between the equatorial and southern Indian Ocean. *Geophysical Research Letters*, *29*(16), 59-1. https://doi.org/10.1029/2001gl014542

Siedler, G., Rouault, M., Biastoch, A., Backeberg, B., Reason, C. J., & Lutjeharms, J. R. (2009). Modes of the southern extension of the east Madagascar current. *Journal of Geophysical Research*, *114*(C1). https://doi.org/10.1029/2008JC004921

Signorini, S. R., Franz, B. A., & McClain, C. R. (2015). Chlorophyll variability in the oligotrophic gyres: Mechanisms, seasonality and trends. *Frontiers in Marine Science*, *2*. https://doi.org/10.3389/fmars.2015.00001

Srokosz, M. A., & Quartly, G. D. (2013). The Madagascar bloom: A serendipitous study. *Journal of Geophysical Research: Oceans*, *118*(1), 14–25. https://doi.org/10.1029/2012JC008339

Srokosz, M. A., Quartly, G. D., & Buck, J. J. (2004). A possible plankton wave in the Indian Ocean. *Geophysical Research Letters*, *31*(13). https://doi.org/10.1029/2004GL019738

Srokosz, M. A., Robinson, J., McGrain, H., Popova, E. E., & Yool, A. (2015). Could the Madagascar bloom be fertilized by Madagascan iron? *Journal of Geophysical Research: Oceans*, *120*(8), 5790–5803. https://doi.org/10.1002/2015JC011075

Tew-Kai, E., & Marsac, F. (2009). Patterns of variability of sea surface chlorophyll in the Mozambique Channel: A quantitative approach. *Journal of Marine Systems*, *77*(1–2), 77–88. https://doi.org/10.1016/j.jmarsys.2008.11.007

Uz, B. M. (2007). What causes the sporadic phytoplankton bloom southeast of Madagascar? *Journal of Geophysical Research*, *112*(C9). https://doi.org/10.1029/2006JC003685

Van der Elst, R., Everett, B., Jiddawi, N., Mwatha, G., Afonso, P. S., & Boulle, D. (2005). Fish, fishers and fisheries of the western Indian Ocean: Their diversity and status. A preliminary assessment. *Philosophical Transactions of the Royal Society A: Mathematical, Physical and Engineering Sciences*, *363*(1826), 263–284. https://doi.org/10.1098/rsta.2004.1492

Van der Elst, R. P., Groeneveld, J. C., Baloi, A. P., Marsac, F., Katonda, K. I., Ruwa, R. K., & Lane, W. L. (2009). Nine nations, one ocean: A benchmark appraisal of the south western Indian Ocean fisheries project (2008-2012). *Ocean & Coastal Management*, *52*(5), 258–267. https://doi.org/10.1016/j.ocecoaman.2009.02.003

Wei, J., Wang, M., Mikelsons, K., Jiang, L., Kratzer, S., Lee, Z., et al. (2022). Global satellite water classification data products over oceanic, coastal, and inland waters. *Remote Sensing of Environment*, *282*, 113233. https://doi.org/10.1016/j.rse.2022.113233

Weimerskirch, H., Corre, M. L., Jaquemet, S., Potier, M., & Marsac, F. (2004). Foraging strategy of a top predator in tropical waters: Great frigate birds in the Mozambique Channel. *Marine Ecology Progress Series*.

Xu, L., Yang, D., Greenwood, J., Feng, X., Gao, G., Qi, J., et al. (2020). Riverine and oceanic nutrients govern different algal bloom domain near the Changjiang estuary in summer. *Journal of Geophysical Research: Biogeosciences*, *125*(10), e2020JG005727. https://doi.org/10.1029/2020JG005727

Yang, K., Meyer, A., Strutton, P. G., & Fischer, A. M. (2023). Global trends of fronts and chlorophyll in a warming ocean. *Communications Earth & Environment*, *4*(1), 489. https://doi.org/10.1038/s43247-023-01160-2

Zhen, G., Shang-Min, L., Jia-Rui, S., Lijing, C., Gen, L., & Jun, Y. (2023). Indian Ocean mixed layer depth changes under global warming. *Frontiers in Marine Science*. https://doi.org/10.3389/fclim.2023.1112713